

Insight into the Kinematic and Microphysical Processes that Control Lightning Jumps

CHRISTOPHER J. SCHULTZ

Department of Atmospheric Science, University of Alabama in Huntsville, and NASA Marshall Space Flight Center, Huntsville, Alabama

LAWRENCE D. CAREY

Department of Atmospheric Science, University of Alabama in Huntsville, Huntsville, Alabama

ELISE V. SCHULTZ

Earth System Science Center, University of Alabama in Huntsville, Huntsville, Alabama

RICHARD J. BLAKESLEE

NASA Marshall Space Flight Center, Huntsville, Alabama

(Manuscript received 3 November 2014, in final form 11 August 2015)

ABSTRACT

A detailed case study analysis of four thunderstorms is performed using polarimetric and multi-Doppler capabilities to provide specificity on the physical and dynamical drivers behind lightning jumps. The main differences between small increases in the total flash rate and a lightning jump are the increases in graupel mass and updraft volumes $\geq 10 \text{ m s}^{-1}$ between the -10° and -40°C isotherms. Updraft volumes $\geq 10 \text{ m s}^{-1}$ increased in magnitude at least 3–5 min in advance of the increase in both graupel mass and total flash rate. Updraft volumes $\geq 10 \text{ m s}^{-1}$ are more robustly correlated to total flash rate than maximum updraft speed over a thunderstorm's entire life cycle. However, peak updraft speeds increase prior to 8 of the 12 lightning jumps examined. Decreases in mean and median flash footprint size during increases in total lightning are observed in all four thunderstorms and are most notable during development stages within the most intense storms. However, this inverse relationship breaks down on larger storm scales as storms mature and anvils and stratiform regions developed with time. Promisingly, smaller flash sizes are still collocated with the strongest updraft speeds, while larger flash sizes are observed within weaker updraft regions. The results herein emphasize the following for lightning jump applications: both the lightning jump sigma level and the resultant magnitude of the total flash rate must be employed in conjunction to assess storm intensity using lightning data. The sigma-level magnitude of the lightning jump is the early warning that indicates that rapid intensification is occurring, while the magnitude of the total flash rate provides insight into the size and maintenance of the updraft volume and graupel mass. These cases serve as conceptual models for future applications of the lightning jump algorithm for hazardous weather monitoring.

1. Introduction

Flash rates and changes in the flash rate are the primary lightning properties related to storm intensity within the literature. Both total flash rate (TFR) and cloud-to-ground (CG) flash rate have been used to assess the potential for a storm to produce severe weather [e.g., Goodman et al. (1988); MacGorman et al. (1989);

Williams et al. (1999); Schultz et al. (2011) and references contained within]. Rapid increases in total lightning (i.e., lightning jumps) are well correlated to increased severe weather potential (e.g., Williams et al. 1999; Schultz et al. 2009, 2011; Gatlin and Goodman 2010; Rudlosky and Fuelberg 2013; Stano et al. 2014). Despite showing strong correlation between lightning jumps and severe weather occurrence, none of the aforementioned studies above provides direct measurements of updraft and microphysical properties at the time of a lightning jump. Thus, the reader is left to infer that the thunderstorm's updraft must increase in

Corresponding author address: Dr. Christopher J. Schultz, UAH/NASA MSFC, 320 Sparkman Dr., Huntsville, AL 35805.
E-mail: christopher.j.schultz@nasa.gov

size and/or magnitude for a lightning jump to occur based on previously reported evidence linking upward trends in kinematic and microphysical properties to increases in total flash rate (e.g., Carey and Rutledge 1996; Lang and Rutledge 2002; Tessendorf et al. 2005; Kuhlman et al. 2006; Deierling and Petersen 2008).

Certainly, numerous studies illustrate good correlation between updraft volume, precipitation mass ice production, and flash rate (e.g., Workman and Reynolds 1949; Dye et al. 1989; Rutledge et al. 1992; Zipser and Lutz 1994; Carey and Rutledge 2000; Boccippio 2002; Lang and Rutledge 2002; Cecil et al. 2005). However, fewer studies provide direct measurements of storm kinematics (particularly updraft properties) and microphysics specifically at the time of lightning jumps (e.g., Carey and Rutledge 1996; Tessendorf et al. 2005; Wiens et al. 2005; Deierling and Petersen 2008; Lund et al. 2009; Calhoun et al. 2013). None of these studies analyzed the impact of these properties in the development of lightning jumps. Additional works in combination provide kinematic and microphysical observations and total lightning observations of the same storm (e.g., Goodman et al. 1988; Tuttle et al. 1989). Furthermore, debate still exists over which updraft property is best correlated to total flash rate. Lang and Rutledge (2002), Kuhlman et al. (2006), and Deierling and Petersen (2008) demonstrate that updraft volume is the kinematic parameter that is consistently well correlated to total flash rate, while Barthe et al. (2010) observed that peak updraft speed was better correlated to the total flash rate than updraft volume when modeling the same storms from Deierling and Petersen (2008).

There are lightning characteristics beyond flash rate that provide information on the internal kinematic and microphysical structure of thunderstorms. Recent work by Bruning and MacGorman (2013) explored the inverse relationship between flash rate and flash area using lightning mapping array data. Bruning and MacGorman provide theoretical arguments for initial breakdown, flash propagation (i.e., extent) and termination using the vector electric field, and the potential and the charge density. Bruning and MacGorman (2013) examined two supercell thunderstorms and showed how the mean and median flash areas decreased as the flash count increased and provided an estimate of the total electrical energy being produced by the storm. Both Bruning and MacGorman (2013) and Calhoun et al. (2013) postulated that the inverse flash rate-extent relationship is an indicator of the kinematic texture of the storms updraft (turbulent vs laminar) using the hypothesis that the regions of the storm with the highest flash rates and smallest flash extents are closest to the strongest, most turbulent updrafts.

Recent observations by Calhoun et al. (2014) demonstrate that operational weather forecasters rate information on a thunderstorm's updraft as one of the highest priorities when making warning decisions. Linkages between lightning jumps and storm kinematics and microphysics provide the necessary bridge by which the forecaster can assess a storm's mixed-phase updraft strength using lightning data. Herein, physical and dynamical ties between lightning characteristics, lightning jump, and storm morphology are discussed using highly detailed case studies of four thunderstorms specifically centered on the time of lightning jump occurrences. The analysis techniques utilize polarimetric, multi-Doppler, and total lightning observations during storm intensification to compare time trends of updraft volume, maximum updraft speed, graupel volume, graupel mass, and total flash rate at the time of lightning jumps within these four thunderstorms. Additionally, updraft characteristics from the multi-Doppler synthesis are used to investigate the inverse total flash rate and flash extent relationship that should be present at the time of the initial rapid increases in total lightning based on the arguments provided by Bruning and MacGorman (2013).

2. Data and methodology

Multiple datasets and analysis techniques are outlined below that are necessary in relating total lightning to kinematic and microphysical observations. The study domain is northern Alabama and south-central Tennessee, where total lightning, polarimetric, and multi-Doppler observations are all available. The cases chosen are four thunderstorms from a variety of morphologies: an ordinary nonjump thunderstorm (e.g., Bringi et al. 1997), a pulse severe multicellular thunderstorm (e.g., Goodman et al. 1988; Williams et al. 1989), an intensifying portion of a quasi-linear convective system (QLCS; Houze 1989; Carey et al. 2005; Coniglio et al. 2011), and the rapid transition from a multicellular thunderstorm to a supercell thunderstorm (e.g., Vasiloff et al. 1986; Stano et al. 2014).

a. Radar data

The University of Alabama in Huntsville's (UAH) Advanced Radar for Operational Research (ARMOR; Schultz et al. 2012; Knupp et al. 2014) and the National Weather Service's (NWS) radar located at Hytop, Alabama (KHTX; Crum and Alberty 1993), are used for this analysis. When their measurements are combined, three-dimensional retrieval of velocity and bulk characterization of hydrometeor type within a thunderstorm is possible. ARMOR is a polarimetric C-band radar

owned and operated collaboratively by UAH and WHNT-TV in Huntsville, Alabama. ARMOR is located at Huntsville International Airport and is operational 24 h a day, seven days a week. ARMOR can be taken out of its default three-tilt scanning mode to collect volumetric data for research analysis. ARMOR has a 1° beamwidth and is run in simultaneous transmit and receive mode (STAR; Scott et al. 2001). KHTX is an S-band radar that was upgraded to polarimetric capabilities in early 2012. KHTX also operates in STAR, has a beamwidth near 1°, and provides radar volume updates every 4–6 min.

Radar data are corrected for attenuation and differential attenuation (Bringi et al. 2001) and aliased velocities are unfolded using the National Center for Atmospheric Research's (NCAR) SOLO, version 3 (Oye et al. 1995), by manual inspection. During this step, ground clutter and sidelobe and second-trip echoes are also removed. Data are then gridded onto a Cartesian coordinate system centered on ARMOR's location of 34.646198°N, 86.771500°W using a grid resolution of 1 km × 1 km × 1 km on a grid of 300 km × 300 km × 19 km (X, Y, Z). A Cressman weighting scheme is implemented using 1-km radius of influence centered at each grid point with NCAR's REORDER software (Oye and Case 1995). Additional manipulation of the data for vertical velocity retrieval and identification of precipitation using polarimetric information is outlined below.

1) MULTIPLE DOPPLER

First, radar volume times between the two radars are required to occur within 2 min of each other. This requirement minimized errors in vertical velocity retrieval due to spatial offsets in a storm's location with respect to each individual radar with time. Also, each storm used in this study is required to have its tallest 0-dBZ echo covered by the volumetric coverage of both ARMOR and KHTX. This is important for minimizing the potential error in the downward integration of the anelastic continuity equation for vertical velocity retrievals. Next, NCAR's Custom Editing and Display of Reduced Information in Cartesian Space (CEDRIC; Mohr et al. 1986) is used to perform multi-Doppler synthesis with a manual input of storm motion. Vertical velocity retrievals are accomplished by taking radial velocity measurements from two or more radars and using a hydrometeor fall speed relationship to solve a set of linear equations (e.g., Armijo 1969; O'Brien 1970; Brandes 1977; Ray et al. 1980; Deierling and Petersen 2008). Horizontal zonal u and meridional v wind components are directly determined from radial velocity measurements from both radars. A linear reflectivity z ($\text{mm}^6 \text{m}^{-3}$)-based terminal fall speed relationship from Marks and Houze (1987) is used in this study, where

$$V_t = 2.6 \times z^{0.107}; \quad T > 0^\circ\text{C} \quad \text{and} \quad (1)$$

$$V_t = 0.817 \times z^{0.063}; \quad T \leq 0^\circ\text{C}. \quad (2)$$

Once these measurements and assumptions are made, vertical velocity retrievals are calculated by integrating the mass continuity equation. For this study, the variational integration technique is used for multi-Doppler synthesis to minimize errors within the retrievals (Matejka and Bartels 1998). This required that the anelastic continuity equation is integrated from an upper and a lower boundary and that the vertical motions at these boundaries are set to 0 m s^{-1} . Upward integration from the lower boundary condition occurs in the lowest three vertical levels of the grid space, and downward integration from the upper boundary occurs in the remaining 14 vertical levels.

Analyses of updraft speed and volume are limited to the mixed-phase region of the thunderstorm (i.e., between the -10° and -40°C isotherms) because the mixed-phase region is where charge development and separation takes place to ultimately lead to electrical breakdown (e.g., Dye et al. 1986; Carey and Rutledge 1996; Bringi et al. 1997; Deierling and Petersen 2008; Calhoun et al. 2013). Updraft volumes above 10 and 15 m s^{-1} and the 98th percentile and maximum updraft speeds are computed from the multi-Doppler Cartesian grids for the entire storm. The 98th percentile updraft speed is used as a quality control metric for the reader to better understand the behavior in the trend of maximum updraft speed (a point measurement).

The multi-Doppler analysis domain provided temporal bounds for the analysis windows chosen for each case. All radar volumes are used when each thunderstorm is located within the line of constant 1.5-km resolution¹ for multi-Doppler lobe configuration (Fig. 1a), the storm is located inside of the 30° beam-crossing angle (Fig. 1b), and the storm's tallest 0-dBZ echo is covered by both KHTX and ARMOR (Fig. 1). The primary focus for this analysis is on lightning jump times. Work by Schultz (2015) has examined trends in kinematic and microphysical properties prior to all increases in total flash rate, and these results are the subject of a future manuscript.

2) GRAUPEL VOLUME AND MASS CALCULATIONS

Particle identification is performed using ARMOR data and NCAR's particle identification (PID) algorithm (Vivekanandan et al. 1999) modified for C-band observations (Deierling et al. 2008; Johnson 2009). This

¹ See Davies-Jones (1979, their Fig. 2) for more information on dual-Doppler spatial resolution by which these lines were derived from for the ARMOR–KHTX dual-Doppler domain.

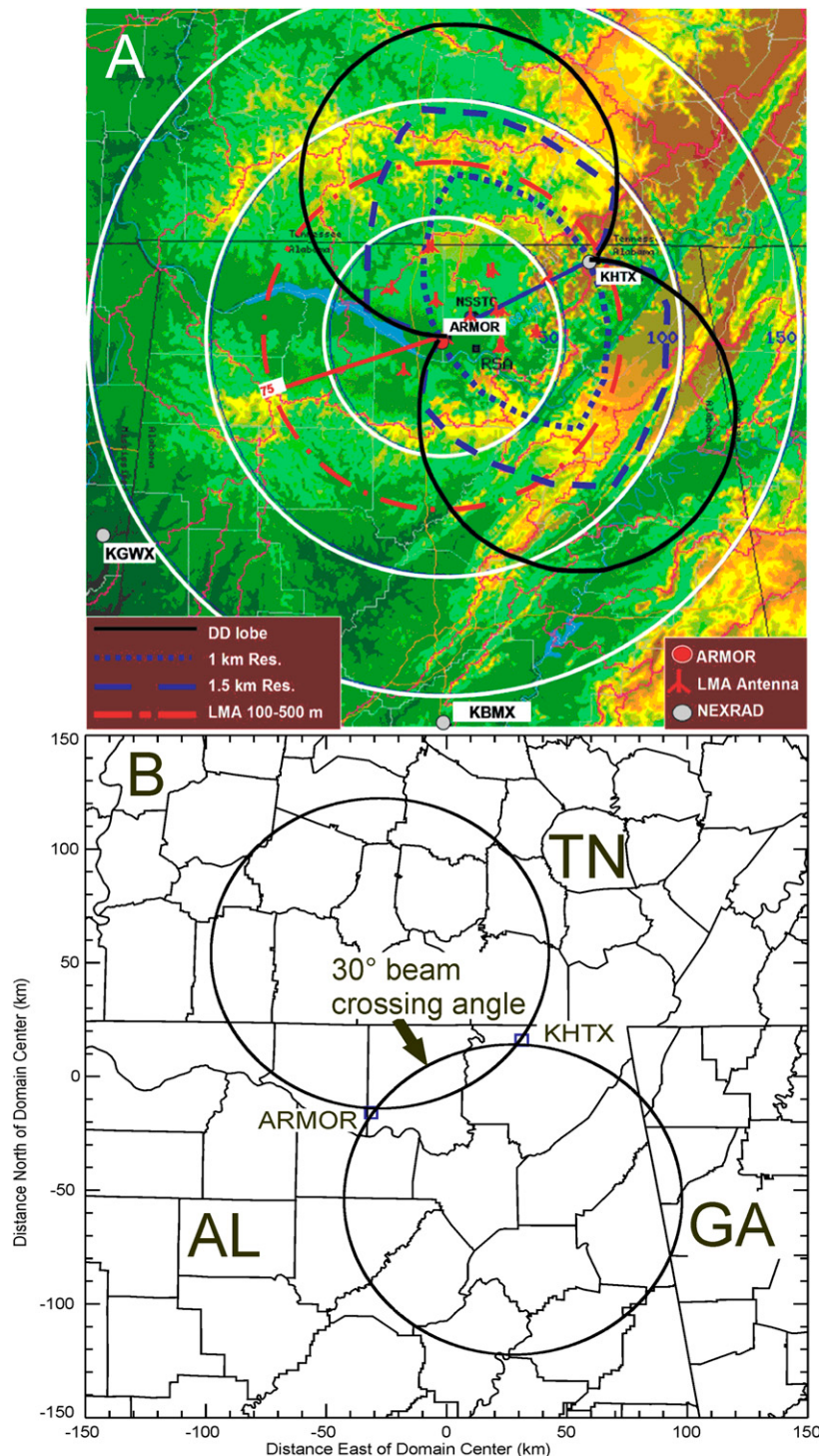


FIG. 1. (a) Black solid lines outline the dual-Doppler (DD) domain, and blue dashed lines indicate the horizontal resolution of the multi-Doppler analysis within the radar domain. Red antennas are for the locations of the LMA sensors centered at the National Space Science and Technology Center (NSSTC), near Redstone Arsenal (RSA), and the red dashed line indicates where vertical position errors in the VHF source information are between 100 and 500 m. White range rings are every 50 km and centered on ARMOR. Other radars that cover the domain are located at Calera, Alabama (KBMX), and Columbus Air Force Base, Mississippi (KGWX). (b) The same multi-Doppler lobes with the 30° beam-crossing angle represented by the oval at $X = 0$ km, $Y = 0$ km, where the two black multi-Doppler circles overlap. TN indicates Tennessee, AL indicates Alabama, and GA indicates Georgia.

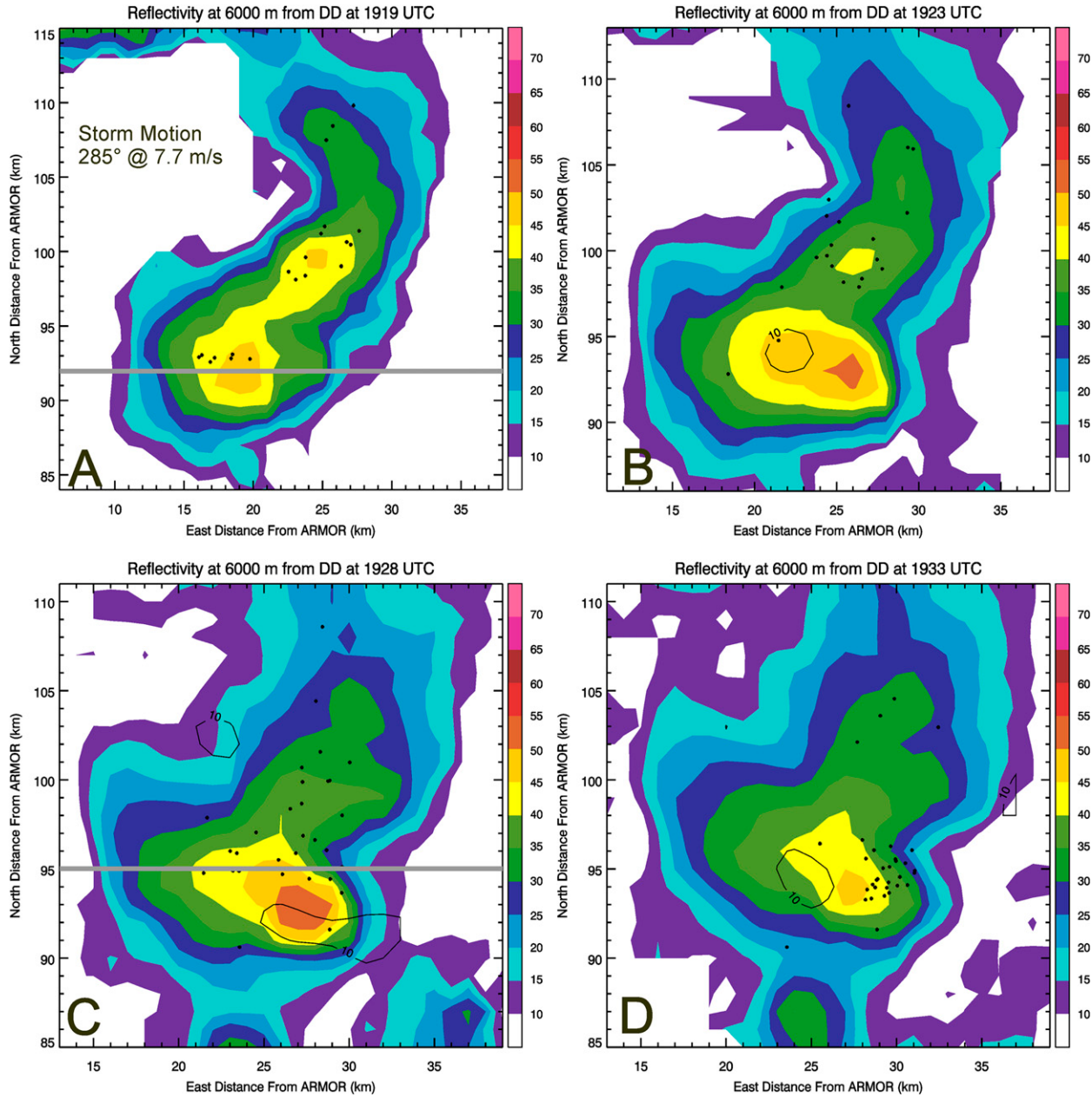


FIG. 2. Reflectivity from ARMOR (dBZ; shaded contours with an interval of 5 dB), vertical velocity (m s^{-1} ; solid black contours with an interval of 10 m s^{-1} starting at 10 m s^{-1}) and lightning initiation points within 3 min of radar volume start time (black dots) at (a) 1919, (b) 1923, (c) 1928, and (d) 1933 UTC at 5 km above radar level (ARL). Gray lines represent cross-sectional locations taken at $Y = 92 \text{ km}$ (1919 UTC) and $Y = 95 \text{ km}$ (1928 UTC) north of ARMOR in Fig. 6.

study is specifically interested in graupel identification because of graupel's strong tie to electrification and lightning production in thunderstorms (e.g., Carey and Rutledge 1996; Saunders et al. 2006; Deierling et al. 2008). NCAR's PID has two categories of graupel: graupel–small hail and graupel–hail–rain mix. Both Deierling et al. (2008) and Bain (2013) found that inclusion of the graupel–hail–rain mix category did not significantly

increase correlations between graupel mass and total flash rate in four thunderstorms in northern Alabama; thus, only the graupel–small hail category was used. Particle identification is performed in 1 km^3 boxes, and the graupel volume is simply the number of boxes identified between -10° and -40°C .

After identification of regions of graupel, graupel mass is calculated using a reflectivity–mass (z – M) relationship

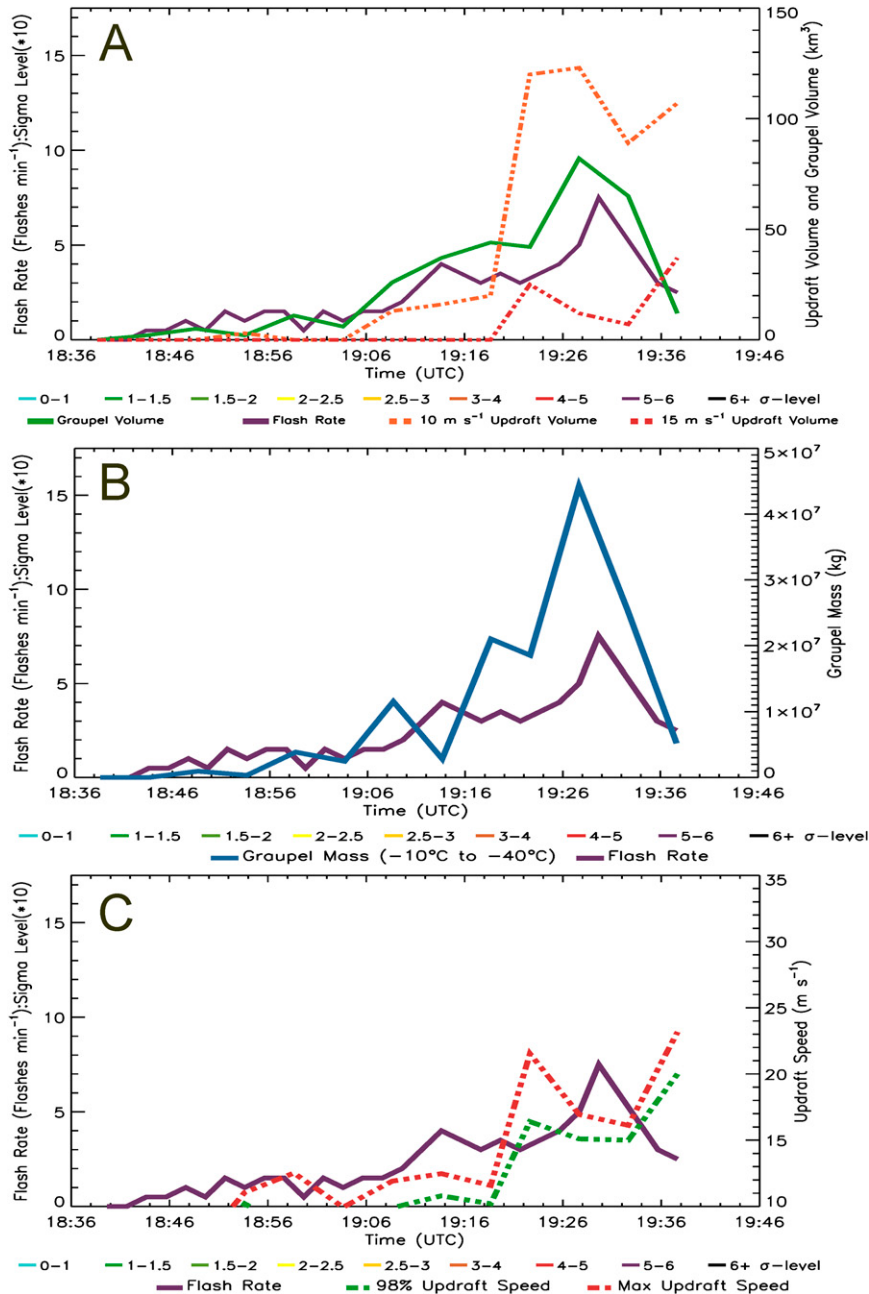


FIG. 3. (a) Updraft volume, graupel volume, and flash rate vs time for an ordinary thunderstorm on 11 Jun 2012 in south-central Tennessee. (b) Graupel mass and flash rate vs time for the same ordinary thunderstorm. (c) Time trend of max updraft speed, 98th percentile updraft speed, and total flash rate. Colored bars in legend refer to sigma-level magnitude multiplied by 10, but results were not calculated because the total flash rate never exceeded 10 flashes min⁻¹.

from Heymsfield and Miller (1988). This relationship is defined as

$$M \text{ (g m}^{-3}\text{)} = 0.0052 \times z^{0.5}, \quad (3)$$

and includes linear reflectivity factor z ($\text{mm}^6 \text{m}^{-3}$). This formula was developed empirically from T-28 aircraft

observations in Heymsfield and Hjelmfelt (1984). Mass is calculated at each 1-km³ pixel identified to be primarily graupel between -10° and -40°C using the z within the pixel. Importantly, Deierling et al. (2008) demonstrated how various z - M relationships show the same trends in graupel mass over time despite having

TABLE 1. Microphysical changes in storm properties during the 15 min prior to the times of sigma levels ≥ 2 or max increase in flash rate. Total flash rate (flashes min^{-1}), sigma level, graupel volume G_{vol} (km^3), change in graupel volume ΔG_{vol} (km^3), graupel mass G_{mass} (kg), and change graupel mass ΔG_{mass} (kg) during previous 15 min prior to the jump time are all computed. Both G_{vol} and G_{mass} are measured between the -10° and -40°C isotherm heights. Numbers in parentheses identify the lightning jump examined in the analysis.

Event	Flash rate	DFRDT	Sigma level	G_{vol}	ΔG_{vol}	$G_{\text{mass}} (\times 10^7)$	$\Delta G_{\text{mass}} (\times 10^7)$
11 Jun 2012	7	1.25	—	82	38	4.42	2.32
3 May 2006 (1)	10	2.50	2.72	41	45	5.24	2.40
3 May 2006 (2)	13	4.25	2.97	111	25	12.3	7.06
3 May 2006 (3)	13	5.00	2.14	143	57	13.0	8.13
12 Mar 2010 (1)	13	3.50	4.72	200	161	29.4	25.6
12 Mar 2010 (2)	31	6.75	2.47	290	220	35.6	31.5
12 Mar 2010 (3)	38	4.00	2.13	516	48	10.6	28.5
12 Mar 2010 (4)	51	6.50	2.41	945	429	86.7	34.0
12 Mar 2010 (5)	85	6.25	2.52	1564	63	138.0	1.73
10 Apr 2009 (1)	21	5.00	7.67	343	109	51.3	25.7
10 Apr 2009 (2)	42	10.75	5.43	343	109	51.3	25.7
10 Apr 2009 (3)	34	4.75	2.05	817	288	91.0	7.10

different magnitudes. Therefore, the use of this z – M relationship is focused on the trend in mass prior to lightning jump occurrences.

3) THUNDERSTORM TRACKING

Objective storm tracking by the Thunderstorm, Identification, Tracking, Analysis, and Nowcasting (TITAN; Dixon and Wiener 1993) algorithm is used to compute storm position and size for each of the storms examined. Thunderstorms are tracked through space and time at the -10°C level, and TITAN output includes the latitude center, longitude center, and a major axis for every radar volume when a feature is observed at the temperature level. This position information is then used to constrain other measurement fields like flash rate, kinematic and microphysical properties, severe storm reports, maximum reflectivity, azimuthal shear, maximum expected size of hail (MESH; Witt et al. 1998; Cintineo

et al. 2012), and vertically integrated liquid (VIL; Greene and Clarke 1972) to individual storms for trend analysis. Maximum reflectivity, azimuthal shear, MESH, and VIL values are each calculated using the algorithms contained within the Warning Decision Support System–Integrated Information (WDSS-II; Lakshmanan et al. 2006) software package using data from KHTX. All severe thunderstorm reports used in these cases are from the National Climatic Data Center's *Storm Data* archive.

b. Lightning data

Total lightning information is collected by the North Alabama Lightning Mapping Array (NALMA; Koshak et al. 2004; Goodman et al. 2005). NALMA is an 11-station array operating between 76 and 82 MHz that is centered at the National Space Science and Technology Center on the campus of UAH. The peak power of

TABLE 2. Kinematic changes in storm properties during the 15 min prior to the times of sigma levels ≥ 2 or max increase in flash rate. Total flash rate (flashes min^{-1}), sigma level, 10 m s^{-1} updraft volume w_{10} (km^3), change in 10 m s^{-1} updraft volume Δw_{10} (km^3), max vertical velocity w_{Max} (m s^{-1}), and change in max vertical velocity Δw_{Max} (m s^{-1}) during the previous 15 min prior to the jump time are all computed. Updraft volumes are measured between the -10° and -40°C isotherm heights. Numbers in parentheses identify the lightning jump examined in the analysis.

Event	Flash rate	DFRDT	Sigma level	w_{10}	Δw_{10}	w_{Max}	Δw_{Max}
11 Jun 2012	7	1.25	—	123	103	16.9	5.3
3 May 2006 (1)	10	2.50	2.72	47	-1	13.2	-0.6
3 May 2006 (2)	13	4.25	2.97	108	62	27.8	14.6
3 May 2006 (3)	13	5.00	2.14	108	62	27.8	14.6
12 Mar 2010 (1)	13	3.50	4.72	331	323	25.2	13.0
12 Mar 2010 (2)	31	6.75	2.47	484	441	20.3	6.0
12 Mar 2010 (3)	38	4.00	2.13	501	108	18.2	-2.9
12 Mar 2010 (4)	51	6.50	2.41	507	6	20.7	2.5
12 Mar 2010 (5)	85	6.25	2.52	598	-179	19.3	-1.4
10 Apr 2009 (1)	21	5.00	7.67	270	127	49.2	19.1
10 Apr 2009 (2)	42	10.75	5.43	270	127	49.2	19.1
10 Apr 2009 (3)	34	4.75	2.05	466	163	28.2	-17.4

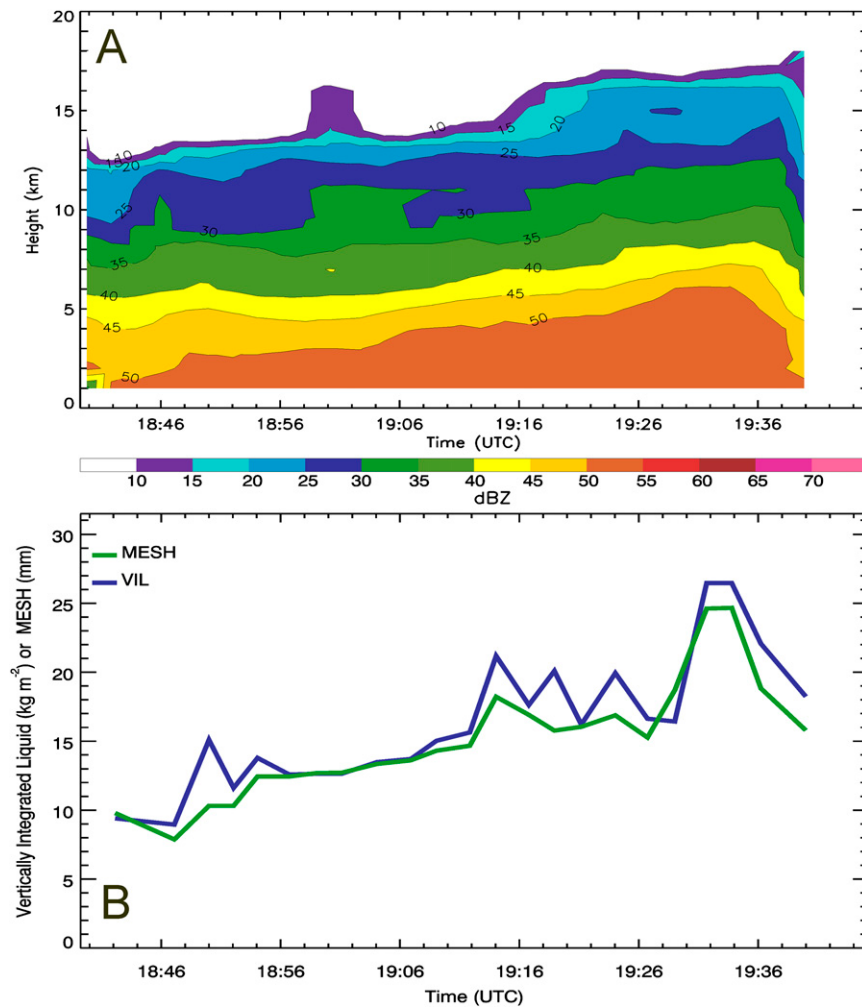


FIG. 4. (a) Time–height of max reflectivity (dBZ; shaded contours with an interval of 5 dB) and (b) time trend of MESH (mm; green line) and VIL (kg m^{-2} ; blue line) between 1843 and 1940 UTC for an ordinary storm on 11 Jun 2012 from KHTX. A lightning jump was not observed with this storm, and the max increase in the total flash rate was at 1928 UTC.

very high frequency (VHF) radiation source points is associated with electrical breakdown and mapped in three dimensions every $80\ \mu\text{s}$. VHF source points are combined into corresponding flashes using a flash-clustering algorithm developed by McCaul et al. (2009). A flash must have a minimum of 10 VHF source points to be considered in this analysis. Flashes are assigned to each storm if their first VHF source point fell within the TITAN-identified storm footprint.

1) THE LIGHTNING JUMP

The 2σ technique from Schultz et al. (2009) is employed to identify lightning jumps within this study. The time of each lightning jump is used to identify the locations of 15-min analysis windows to characterize kinematic and microphysical properties of each

thunderstorm leading up to lightning jump occurrence. However, the lightning jump output is no longer represented by a single point or color for jump occurrence. Instead, any increase in total flash rate is characterized by its sigma level. A sigma level is represented by rearranging the lightning jump equation and taking the ratio of the time rate of change of the total flash rate (DFRDT;² Schultz et al. 2009, 2011; Chronis et al. 2015) and the standard deviation σ calculated from the five previous DFRDT periods or

²The reader is referred to appendix A of Schultz et al. (2011) or the methodology in Chronis et al. (2015) for more details on the lightning jump configuration.

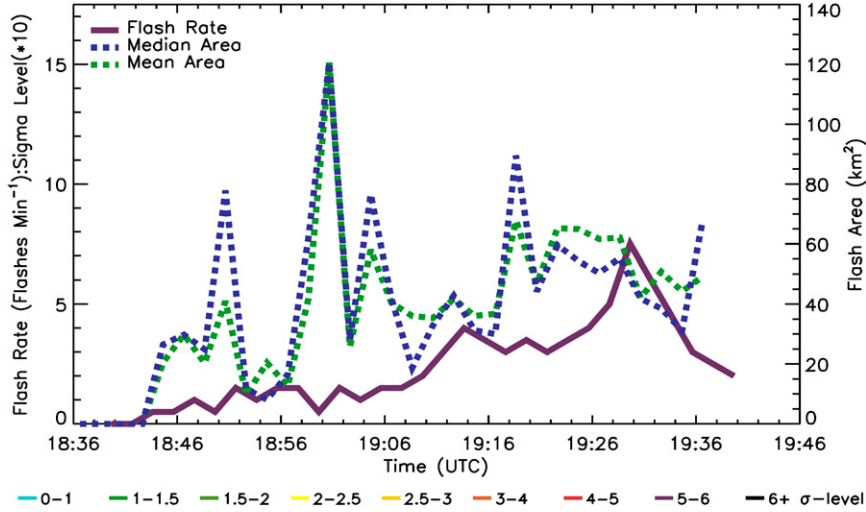


FIG. 5. Mean (green dashed line) and median (blue dashed line) flash area and flash rate (solid purple line) vs time for an ordinary thunderstorm on 11 Jun 2012 in south-central Tennessee. Colored bars in legend refer to sigma-level magnitude, but for this case the sigma level was not calculated because the total flash rate never exceeded $10 \text{ flashes min}^{-1}$.

$$\text{sigma level} = \text{DFRDT}_{t_0}/\sigma(\text{DFRDT}_{t-2,t-4,t-6,t-8,t-10}), \quad (4)$$

where t is time. Thus, a previously defined 2σ jump has a sigma level of 2. Sigma levels are calculated once the total flash rate reaches the lightning jump algorithm activation threshold of $10 \text{ flashes min}^{-1}$ (Schultz et al. 2009). This method is currently being tested both in research and operational applications (e.g., Chronis et al. 2015; Calhoun 2015; Schultz 2015).

The advantage of this new presentation of the lightning jump algorithm information is twofold. First, this presentation method provides a continuous color-coded visual representation of all flash rate increases relative to the storm's recent flash rate history (Calhoun 2015). Therefore, the lightning jump output is not limited to a single time when a jump has occurred like the previous visualization of the algorithm, allowing the end user to have the flexibility to understand how all increases in total flash rate compare to each other in time within a single thunderstorm. Furthermore, the magnitude of the sigma level can be used to assess the significance of the flash rate increase within the storm (e.g., 2σ - vs 8σ -level increase). Sigma-level occurrences of 2.0 and higher are the focus for this paper because they represent a lightning jump. Current work by Schultz (2015) illustrates the kinematic and microphysical changes at all positive sigma levels (i.e., any flash rate increase) and addresses the physical-dynamical significance of the 2σ level beyond the case study analysis of this paper.

2) FLASH SIZE VERSUS FLASH RATE

Flash area (i.e., flash footprint) calculations are made using the convex hull methodology outlined in Bruning and MacGorman (2013).³ Mean and median storm-based flash footprint sizes are calculated in 2-min increments during the analysis window. Additionally, vertical cross sections of mean flash footprint size (km^2) are created to illustrate the spatial proximity of flash size to updraft location, updraft intensity, and reflectivity features [e.g., bounded weak-echo regions (BWER); overshooting echo tops]. The location of each cross-sectional slice is centered on the strongest updraft magnitude within the storm. Flashes within 3 min and $\pm 5 \text{ km}$ of this cross-sectional slice (into and out of the page) are used to calculate mean flash size in the two-dimensional cross section. Thus, each $1 \text{ km} \times 1 \text{ km}$ pixel in the cross section represents a volume of $1 \text{ km} \times 1 \text{ km} \times 10 \text{ km}$ in three-dimensional space. Each flash that passes through the $1 \text{ km} \times 1 \text{ km} \times 10 \text{ km}$ volume is used to determine the value of the mean flash size of each pixel in the vertical cross sections.

3. Results

The observations below are used to demonstrate the connection between lightning characteristics, lightning

³ An example of placing a convex hull around an LMA-derived flash is found in Bruning and MacGorman (2013, their Fig. 2).

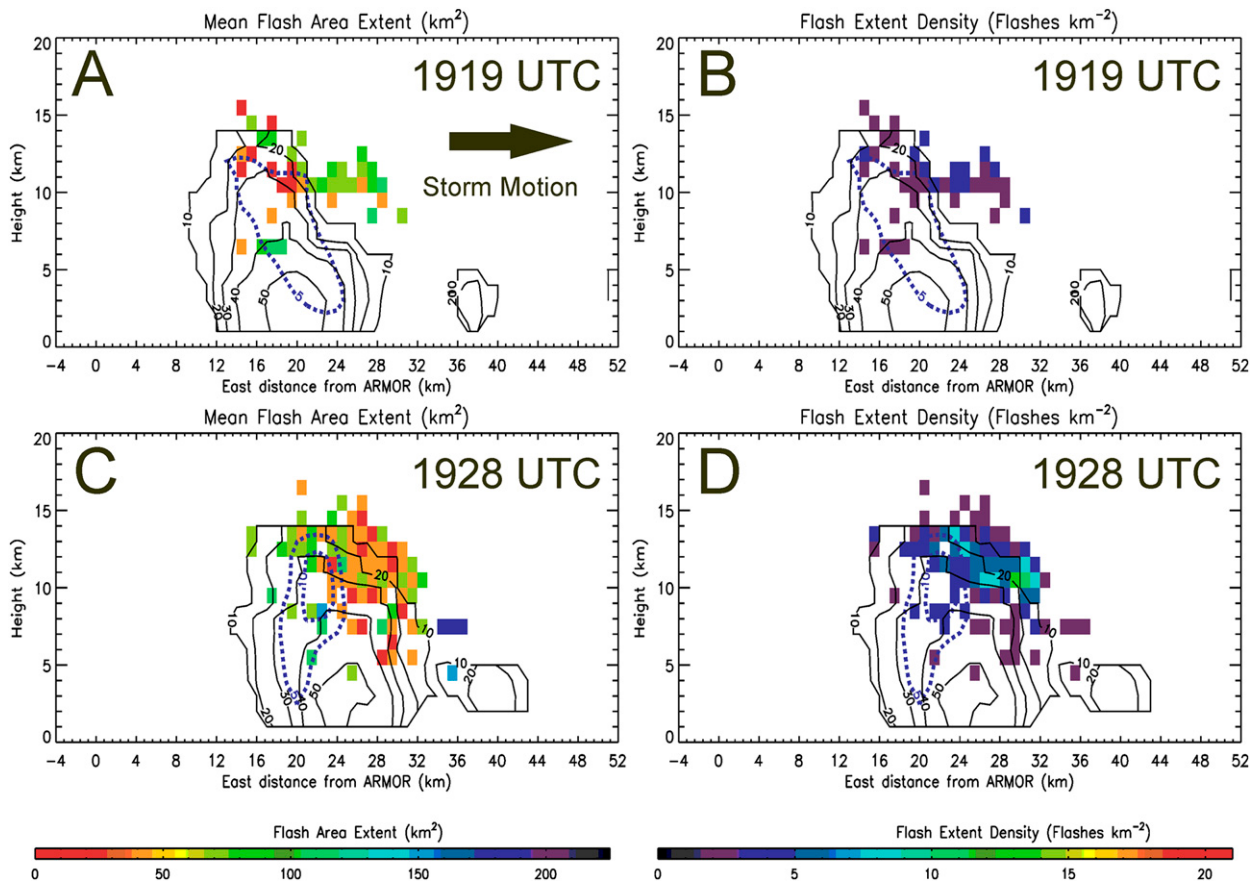


FIG. 6. (a) Mean flash footprint size for the ordinary storm at 1919 UTC 11 Jun 2012 at $Y = 92$ km north of ARMOR. (b) Flash extent density at 1919 UTC 11 Jun 2012 within 5 km of the cross-sectional location of $Y = 92$ km north of ARMOR. (c) Mean flash footprint size at 1928 UTC 11 Jun 2012 at the time of the largest increase in total lightning at $Y = 95$ km north of ARMOR. (d) Flash extent density at 1928 UTC 11 Jun 2012 within 5 km of the cross-sectional location of $Y = 95$ km north of ARMOR. Reflectivity from ARMOR (dBZ; solid contours with an interval of 10 dBZ starting at 10 dBZ) and vertical velocity ($m s^{-1}$; blue dashed contours starting at $5 m s^{-1}$ with an interval of $10 m s^{-1}$ after $10 m s^{-1}$) are overlaid on the mean flash footprint size and flash extent density information.

jumps, and radar-based observations of storm intensity. Detailed examples within this work contain kinematic and microphysical trends at times of lightning jumps (i.e., sigma levels ≥ 2). Included are cases from a non-severe and nonjump multicellular storm, a severe multicellular thunderstorm that contains lightning jumps, a rapidly intensifying segment of a QLCS, and a developing supercell.

a. Case 1: Ordinary thunderstorm without a lightning jump

Presented here is a case from 11 June 2012 during the Deep Convective Clouds and Chemistry Experiment (DC3; Barth et al. 2014; see Fig. 2). The largest increase in the total flash rate with this storm is $2 \text{ flashes min}^{-2}$ at 1928 UTC and this time is the focus of this analysis. During the 14 min prior to the maximum increase, the $10 m s^{-1}$ updraft volume within

the mixed-phase region increases from 16 to 123 km^3 , the $15 m s^{-1}$ volume increases from 0 to 25 km^3 , and the mixed-phase graupel mass doubles from 2.1×10^7 to $4.42 \times 10^7 \text{ kg}$ (Fig. 3; Tables 1 and 2). The $10 m s^{-1}$ updraft volume increases by 6.5 times its original size between 1914 and 1924 UTC (Fig. 3b). Peak (98th percentile) updraft speeds also increase from 11.6 (9.8) to 16.9 (14.2) $m s^{-1}$ between 1914 and 1933 UTC (Fig. 3c).

Radar-based intensity metrics used for severe storm analysis show this storm has low potential for producing severe weather (Fig. 4). A slight increase in height of the 50-dBZ reflectivity isosurface is noted during the time of the increase in the total flash rate as seen with cases that contained lightning jumps (e.g., Schultz et al. 2011; Metzger and Nuss 2013; Fig. 4a). In fact, the peak reflectivity for this storm during the period does not exceed 55 dBZ. An upward trend occurs in the MESH

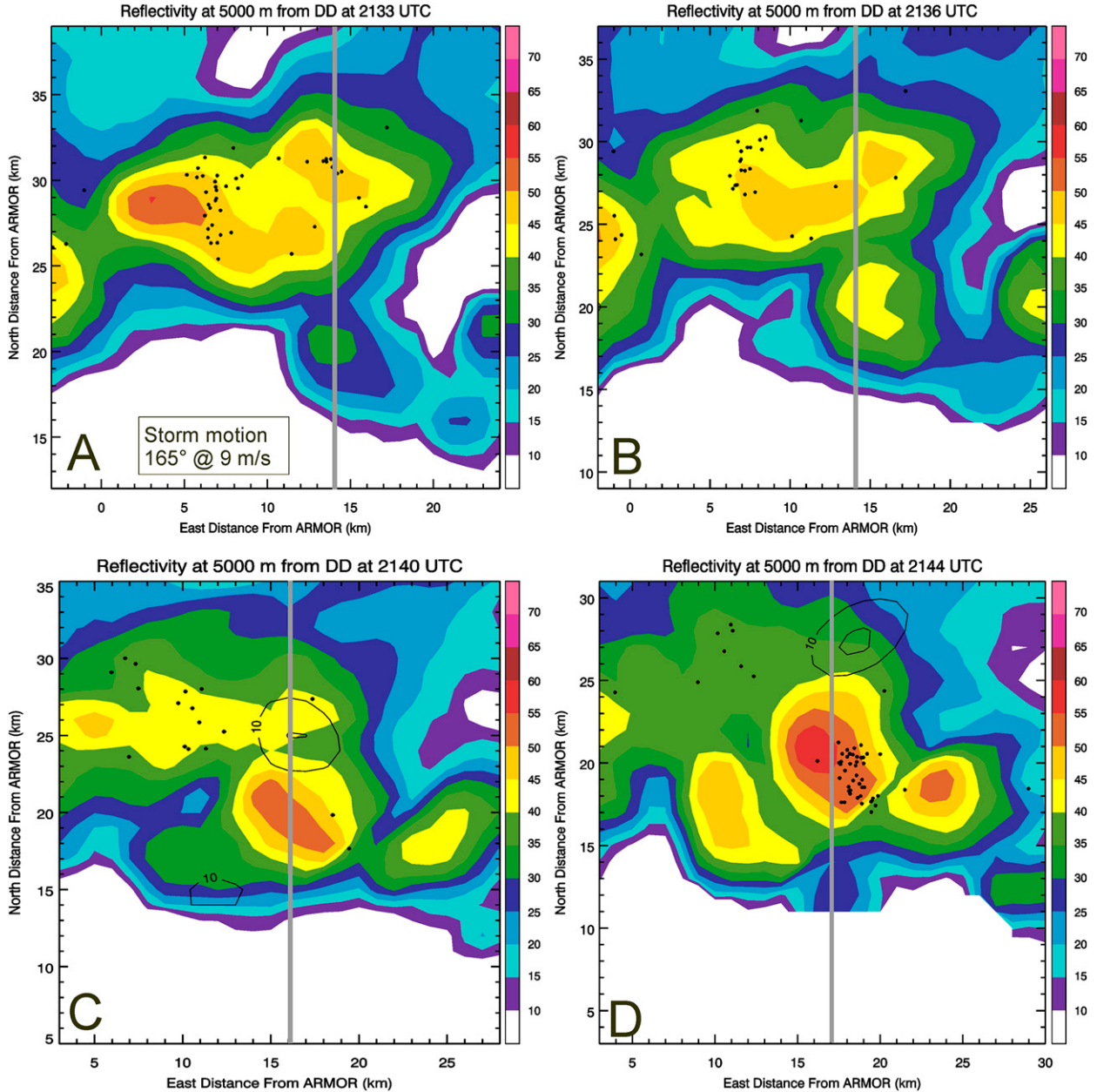


FIG. 7. Reflectivity from ARMOR (dBZ; shaded contours with an interval of 5 dB), vertical velocity (m s^{-1} ; solid black contours with an interval of 10 m s^{-1} starting at 10 m s^{-1}) and lightning initiation points within 1 min of radar volume start time (black dots) at (a) 2133, (b) 2136, (c) 2140, and (d) 2144 UTC at 5 km ARL. Gray lines represent cross-sectional locations taken at $X = 14 \text{ km}$ (2133 and 2136 UTC), $X = 16$ (2140 UTC), and $X = 17 \text{ km}$ (2144 UTC) east of ARMOR in Figs. 10 and 12.

from 14 to 25 mm and VIL rises from 16 to 28 kg m^{-2} between 1928 and 1933 UTC (Fig. 4b).

A modest decrease in both median and mean flash size is observed during the increase in updraft properties during this same period (Fig. 5). Between 1919 and 1927 UTC the average mean and median flash areas are 61.7 and 59.6 km^2 , respectively. During the period in which the flash rate increases (1927–1931 UTC) the averages of

the mean and median flash areas fall to 49.7 and 47.0 km^2 , respectively.

Cross sections at 1919 and 1928 UTC also provide spatial context to this reduction in the flash footprint (Fig. 6). At 1919 UTC the mean flash footprints near the 5 m s^{-1} updraft core are on the order of $\leq 20 \text{ km}^2$, while larger flash footprints on the order of $30\text{--}60 \text{ km}^2$ are found downwind from the updraft (Fig. 6a). As the

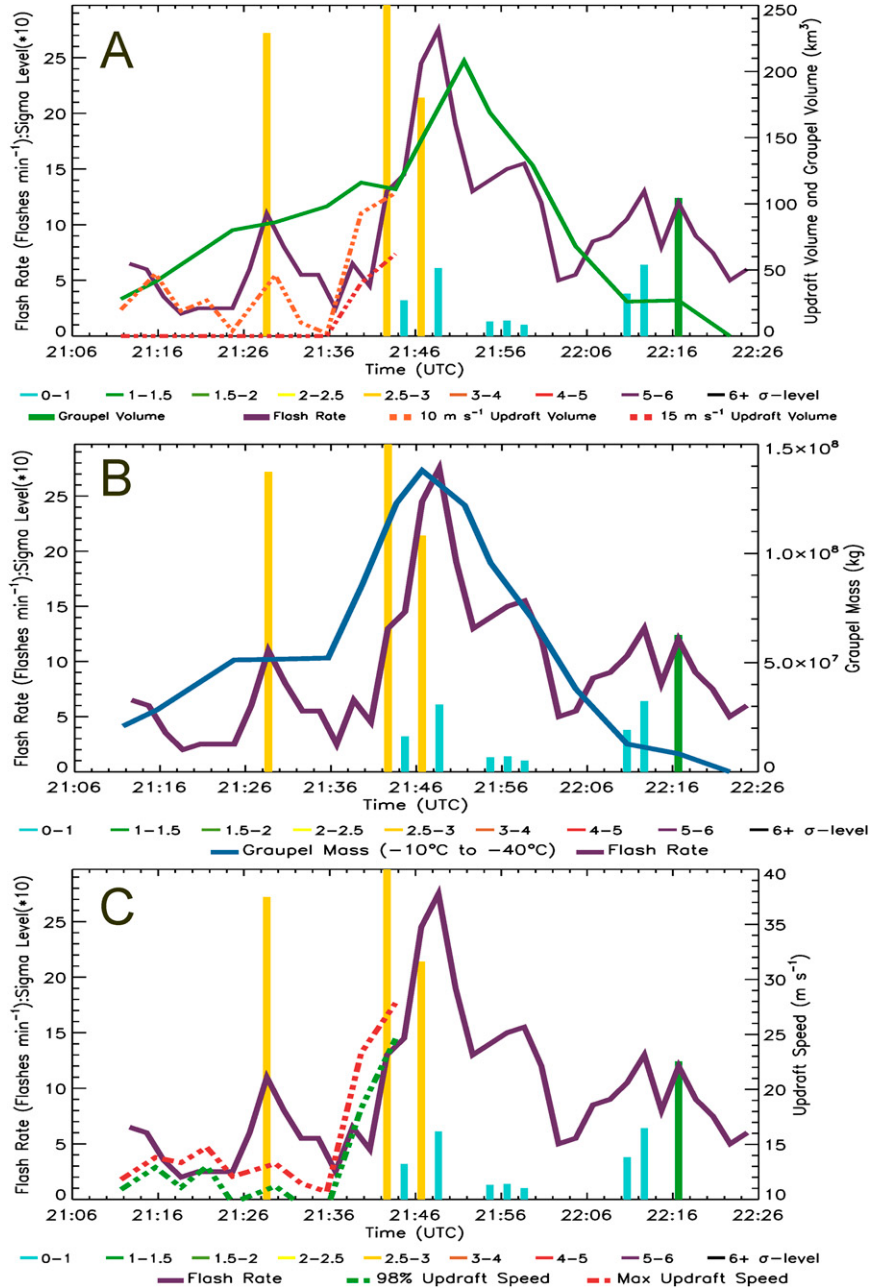


FIG. 8. As in Fig. 3, but for a severe multicellular thunderstorm on 3 May 2006 in northern Alabama. Colored bars indicate sigma-level magnitudes, and color corresponds to the range of values within the legend. Sigma levels have been multiplied by 10 for visibility.

updraft speed, updraft volume, and total flash rate increase at 1928 UTC, the number of 1-km² footprint regions that contain mean flash areas below 20 km² increases from 16 to 45 pixels (Fig. 6c). The number of flashes per pixel also increases by as much as 10 flashes per pixel (Fig. 6d), illustrating the collocation between smaller flash sizes and the location of higher total flash rates.

b. Case 2: Multicellular thunderstorm with a lightning jump

This case captures the rapid intensification of a 1.9-cm hail-producing multicellular cluster over northern Alabama on 3 May 2006 (Fig. 7). The analysis period for this multicellular cluster runs between 2114 and 2144 UTC. This first lightning jump within this multicellular cluster

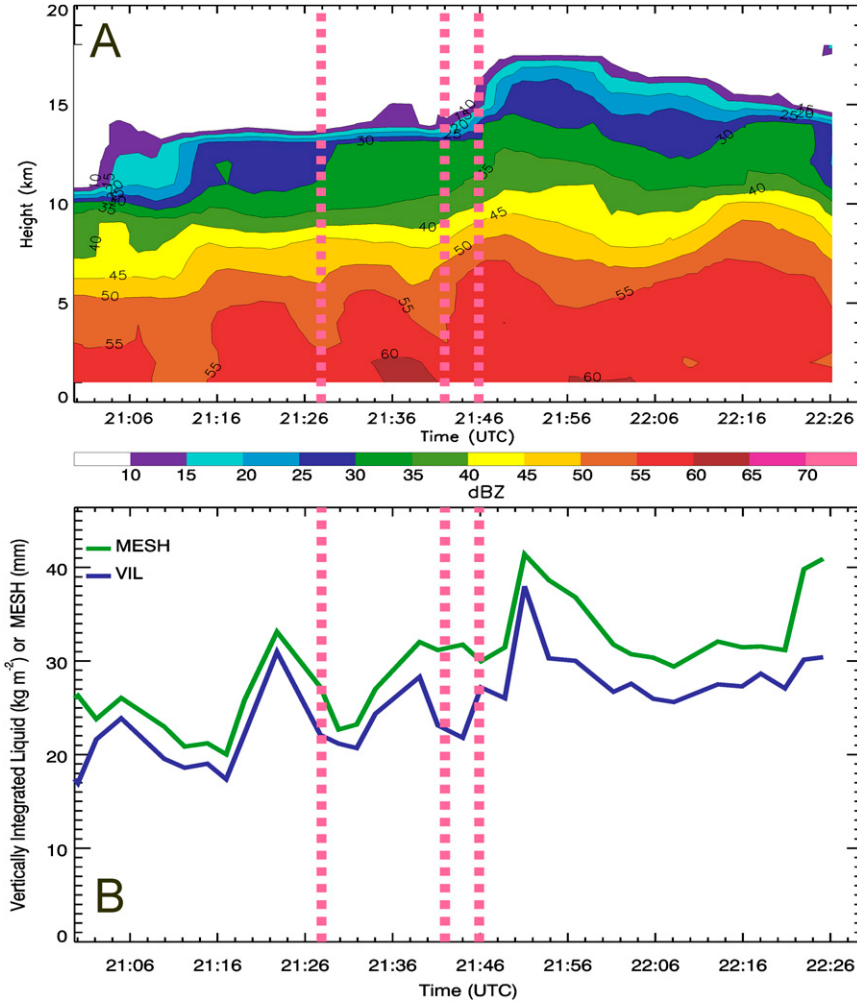


FIG. 9. As in Fig. 4, but for the multicellular storm between 2056 and 2226 UTC 3 May 2006. The lightning jump times were 2128, 2142, and 2146 UTC (vertical dashed pink lines).

occurs at 2128 UTC. A sigma level of 2.72 was registered as the total flash rate increases from 3 to 10 flashes min^{-1} . Prior to 2130 UTC the peak 10 m s^{-1} volume was 40 km^3 and the peak graupel mass was $2 \times 10^7 \text{ kg}$. The largest 10 m s^{-1} volume change is 30 km^3 , and the largest change in graupel mass was $4 \times 10^6 \text{ kg}$ (Fig. 8). The 55-dBZ reflectivity isosurface maximum height grows from 2 to 5 km in the 15 min prior to jump occurrence, and a 60-dBZ isosurface emerges at the 2-km level by 2136 UTC (Fig. 9). MESH increases to 30 mm just prior to the first lightning jump at 2128 UTC as the 55-dBZ isosurface grows to 5 km and maintains its height between 2116 and 2126 UTC. Zero hail reports are received from this multicellular cluster at this time.

At 2133 UTC, new storm growth ($X = 14 \text{ km}$, $Y = 20 \text{ km}$) begins southeast of the existing mature convection ($X = 8 \text{ km}$, $Y = 28 \text{ km}$) in this multicellular cluster (Fig. 7a). At 2133 UTC two flashes initiate within the

location of weaker vertical motion ($w < 10 \text{ m s}^{-1}$; $Y = 30 \text{ km}$, $Z = 4 \text{ km}$), while the developing portion of the storm ($Y = 20 \text{ km}$, $Z = 4 \text{ km}$) has zero lightning flashes associated with it (Fig. 10a). At 2136 UTC, zero flash initiations are found along this entire cross section, and the only lightning activity near the cross section is from the preexisting mature convection ($w < 10 \text{ m s}^{-1}$) at $X = 8 \text{ km}$, $Y = 29 \text{ km}$ (Figs. 7b, 10b). During the next 6 min, growth of the mixed-phase updraft volume $\geq 10 \text{ m s}^{-1}$ is noted within the cell at $X = 16 \text{ km}$, $Y = 25 \text{ km}$. Also, between 2136 and 2140 UTC the 40-dBZ contours merge (Figs. 7b,c and 10b,c). Graupel mass and the 10 and 15 m s^{-1} updraft volumes quadruple from their values at 2136 UTC (Fig. 8a,b).

Flashes initiate downwind of this intense updraft growth (e.g., $X = 19 \text{ km}$, $Y = 19 \text{ km}$; Figs. 7d, 10d). A sigma level of 2.97 was observed at 2142 UTC as the total flash rate increases from 3 to 13 flashes min^{-1} in

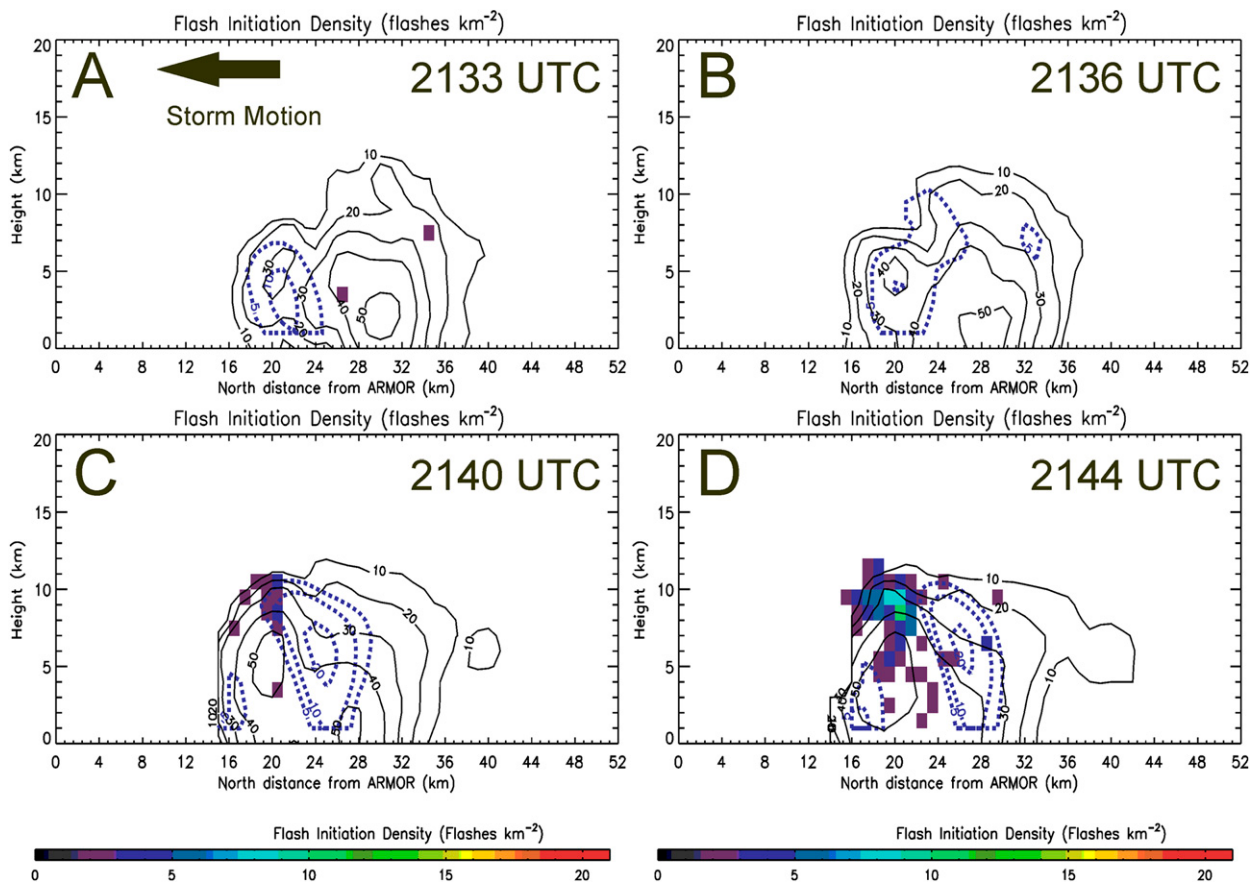


FIG. 10. Flash initiation density for four times leading up to the lightning jump at 2142 UTC: (a) 2133 ($X = 14$ km east of ARMOR), (b) 2136 ($X = 14$ km east of ARMOR), (c) 2140 (16 km east of ARMOR), and (d) 2144 UTC (17 km east of ARMOR). Reflectivity from ARMOR (dBZ; solid black contours at an interval of 10 dB starting at 10 dBZ) and vertical velocity (m s^{-1} ; blue dashed contours starting at 5 m s^{-1} with an interval of 10 m s^{-1} after 10 m s^{-1}) are overlaid on the flash initiation density information.

2 min. The sigma level remained positive for the next 6 min, and a third lightning jump was observed at 2146 UTC (sigma level = 2.14; Fig. 8). This prolonged period of sigma levels with positive magnitudes culminated when the total flash rate peaked at 29 flashes min^{-1} at 2148 UTC. The last time the updraft volume is computed is 2144 UTC, before the storm moves out of the 30° beam-crossing angle and into the region near the multi-Doppler baseline (Fig. 1b). At this point the 10 m s^{-1} updraft volume in the multicellular cluster exceeds 100 km^3 , and the storm total graupel mass exceeds $1.23 \times 10^8 \text{ kg}$ at 2146 UTC (jump 3; Tables 1 and 2). At 2155 UTC, 1.9-cm hail is reported in Huntsville.

It is important to note that multiple updrafts within the multicellular cluster contributed to the overall magnitude and dramatic increase in kinematic and microphysical properties. The 10 m s^{-1} updraft volume increases from 2 to 73 km^3 with this cluster between 2136 UTC and the lightning jump time of 2142 UTC, and eventually reaches as high as 105 km^3 before the storm

moves into the region near the baseline at 2148 UTC (Fig. 8a). At 2136 UTC, the graupel mass is at $1.3 \times 10^7 \text{ kg}$, and by 2144 UTC, the estimated graupel mass had exceeded $8 \times 10^7 \text{ kg}$, eventually peaking at $1.3 \times 10^8 \text{ kg}$ at 2147 UTC (Fig. 8b). Importantly, the mixed-phase graupel mass increases by nearly 8 times its value during this period. The maximum vertical velocity within the storm doubles, increasing from 10.7 m s^{-1} to 23.3 m s^{-1} by 2140 UTC (Fig. 8c). The maximum vertical velocity observed prior to the storm entering the region outside of the optimal 30° beam-crossing angle near the baseline of the multi-Doppler domain was 28 m s^{-1} at 2144 UTC. From 2140 to 2146 UTC, the 55-dBZ reflectivity isosurface shows its largest vertical growth from 3 to 6 km and the 35-dBZ reflectivity isosurface also increases in height from 10 to 12 km (Fig. 9a). Furthermore, MESH values increase by 15 mm from 25 to 40 mm between 2135 and 2150 UTC, with the largest growth in magnitude occurring at 2146 UTC, just prior to hail fall at 2152 UTC (Fig. 9b). Another 60-dBZ

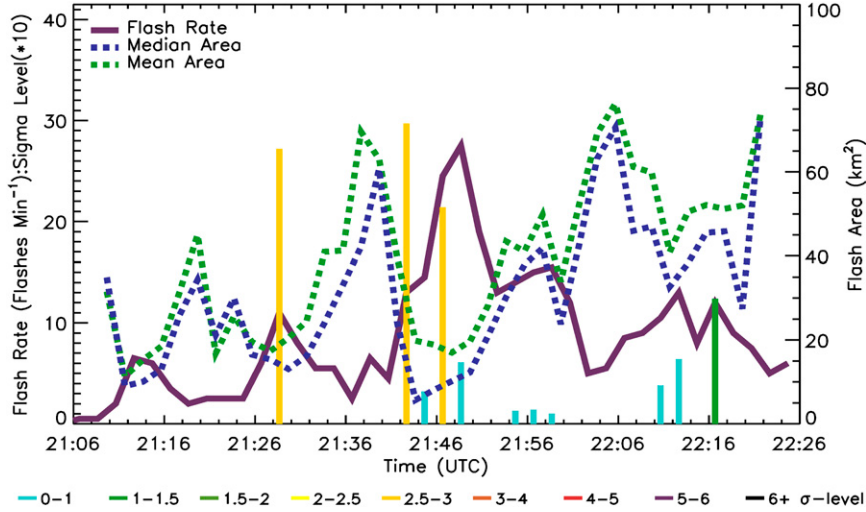


FIG. 11. As in Fig. 5, but for a severe multicellular thunderstorm on 3 May 2006 in north-central Alabama. Colored bars indicate sigma-level magnitudes, and color corresponds to the range of value within the legend. Sigma-level values have been multiplied by 10 for visibility.

reflectivity isosurface emerges at 1 km at 2156 UTC as MESH peaks at 40 mm.

Flash size evolution is more complicated with this case because there are multiple updrafts at various stages of their lifetime contributing to the overall charge structure of the multicellular storm. Three notable decreases in mean and median flash size are observed with increasing total flash rate during the multicellular cluster's lifetime (Fig. 11; 2120, 2140, and 2208 UTC). The total flash rate decreases and the mean flash footprint size increases as updrafts within the cluster weaken. The most notable decrease occurs between 2134 and 2142 UTC. At 2136 UTC the mean and median flash footprint sizes are 48.8 and 36.0 km^2 , respectively. At the time of the lightning jump at 2142 UTC, the averages of the mean and median flash areas drop to 21.5 and 11.46 km^2 . Smaller mean and median flash footprint sizes are observed with this multicellular cluster than with the storm in section 3a, with the main kinematic difference between the two storms being a larger maximum updraft speed in this multicell system (Figs. 3c, 8c).

Figure 12 highlights the intricate flash size and flash rate relationship between multiple updrafts in the multicellular storm. At 2133 UTC, the smallest flash footprints and highest flash rates are located along the same Y location as the tallest portion in this multicellular cluster (Figs. 7a, 12a). Moving forward to 2136 UTC there are zero flash initiations within the cross section (Fig. 10b) and flashes from the more mature convective portion of the cluster at $X = 8 \text{ km}$, $Y = 28 \text{ km}$ traverse within 5 km of the cross section (Figs. 7b, 12b). At 2140 UTC lightning develops between the two regions of 10 m s^{-1} updraft, and consists of several flashes that have mean

and median areas that are smaller than 20 km^2 (Figs. 10c, 12c). Larger flash footprints are located upwind of the intense updraft at $Y = 25 \text{ km}$, $Z = 5 \text{ km}$ within the decaying portion of the multicellular cluster. This observation infers a weaker and broader updraft (Bruning and MacGorman 2013, their Fig. 1a). Similarly, the smaller mean footprint sizes are in the inferred turbulent region just downwind of the most intense updraft. At 2144 UTC, more flash initiations and smaller flash footprints continue to be found just downwind of the main intense mixed-phase updraft in this multicellular thunderstorm, while larger flashes extend northward into the older portion of the complex where weaker updrafts (hence, weaker inferred turbulence) are located (Figs. 10d, 12d).

c. Case 3: Rapidly developing bowing segment within a QLCS with lightning jumps

On 12 March 2010, northeastern Alabama saw a prolific hail-producing segment of a QLCS that moved through during the late morning hours (Fig. 13). Hail up to 4.4-cm in diameter coupled with 38 m s^{-1} winds broke windows and damaged roofs and siding in Marshall, Jackson, and DeKalb Counties. The initial intensification of this bowing segment within the QLCS is captured as the system moves through the multi-Doppler domain between 1500 and 1600 UTC. During the early portion of this period this section of the QLCS rapidly intensifies as the first two lightning jumps occur and its midlevel reflectivity structure takes on a backward "C" shape, indicating potentially strong convective wind development (Fig. 14).

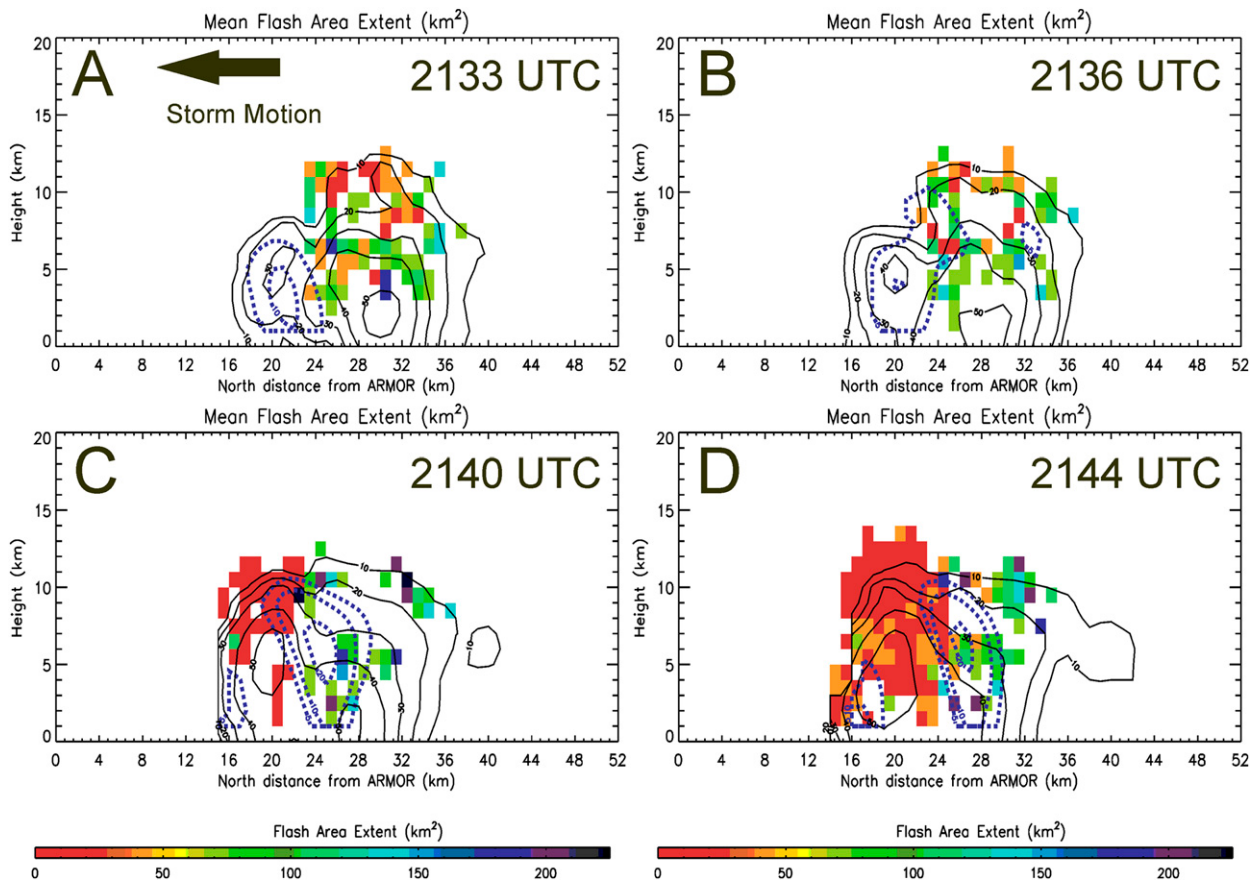


FIG. 12. Mean flash footprint size for a severe multicellular thunderstorm on 3 May 2006 in north-central Alabama. Cross-sectional locations are the same as in Fig. 10. Reflectivity from ARMOR (dBZ; solid black contours at an interval of 10 dBZ starting at 10 dBZ) and vertical velocity (m s^{-1} ; blue dashed contours starting at 5 m s^{-1} with an interval of 10 m s^{-1} after 10 m s^{-1}) are overlaid on the flash initiation density information.

The first lightning jump is observed at 1502 UTC as the total flash rate increases from 6 to 13 flashes min^{-1} . This jump has a sigma-level magnitude of 4.72 (Fig. 15). The 10 m s^{-1} updraft volume dramatically increases from 43 to 331 km^3 (Fig. 15a). The 15 m s^{-1} updraft volume is nonexistent prior to the jump, but grows to 114 km^3 by 1503 UTC. The mixed-phase graupel volume grows from 70 to 200 km^3 , and graupel mass grows from 4.1×10^7 to $3.0 \times 10^8 \text{ kg}$ (Fig. 15b). The peak (98th percentile) updraft speed doubles from 12 (9) to 25 (18) m s^{-1} , leading up to this first jump (Fig. 15c). This first jump is accompanied by an increase in the height of all reflectivity isosurface heights greater than 35 dBZ, with the maximum height of the 55-dBZ reflectivity isosurface increasing by as much as 2 km between 1503 and 1509 UTC (Fig. 16a). MESH doubles from 25 to 55 mm during this period and there is the first emergence of a 60-dBZ reflectivity isosurface at 2 km by 1506 UTC (Fig. 16b).

Between 1503 and 1509 UTC, the 10 and 15 m s^{-1} updraft volumes continue to grow, increasing by 153 and

21 km^3 , respectively (Fig. 15a). Graupel volume also rapidly increases in magnitude from 200 to 290 km^3 (Fig. 15b). The total flash rate increases from 6 to 31 flashes min^{-1} indicated by three consecutive 2-min periods with positive sigma levels of 1.60, 0.75, and 2.50 (i.e., a second jump) between 1508 and 1512 UTC. At 1509 UTC the 10 and 15 m s^{-1} updraft volumes leveled off at 500 and 135 km^3 , respectively; however, the graupel volume continues to increase to 282 km^3 . Between 1509 and 1515 UTC, the graupel mass increases from 3.0×10^8 to $4.7 \times 10^8 \text{ kg}$. The first reports of severe weather were received at 1525 UTC, as hail of a quarter size and larger fell in Lake Guntersville, Alabama; numerous trees were toppled within Guntersville State Park. This hail fall was accompanied by the development of reflectivity values in excess of 65 dBZ at 1–2 km and peak MESH values approaching 60 mm (Fig. 16).

Three additional lightning jumps are also noted at 1528, 1542, and 1600 UTC. The third and fourth lightning jumps at 1528 and 1542 UTC have sigma levels of

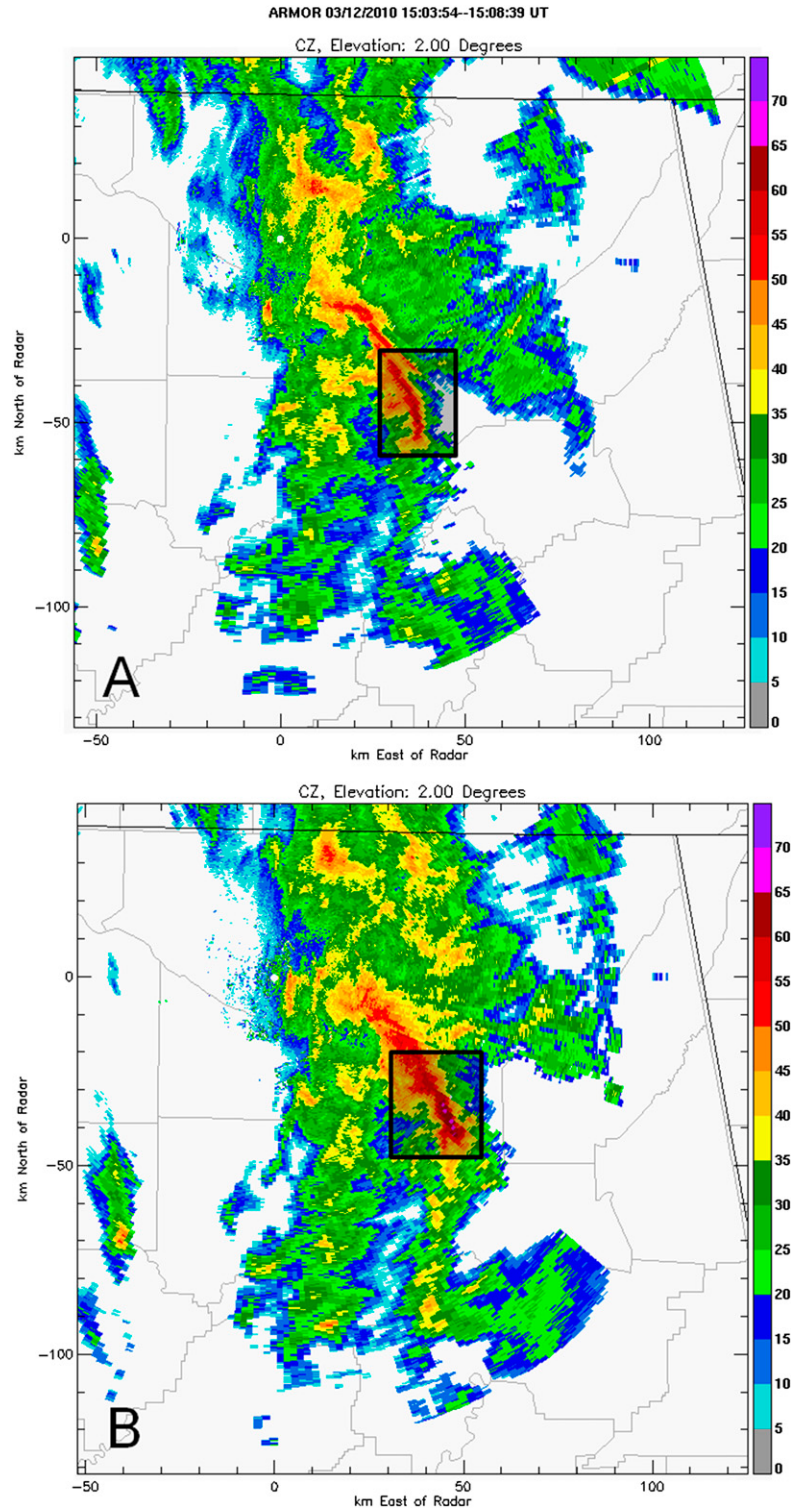


FIG. 13. PPI of reflectivity (dBZ; shaded contours with an interval of 5 dB) from ARMOR at (a) 1503 and (b) 1515 UTC 12 Mar 2010. Black box indicates TITAN-identified portion of the QLCS that underwent rapid intensification and produced the majority of the severe weather with this system.

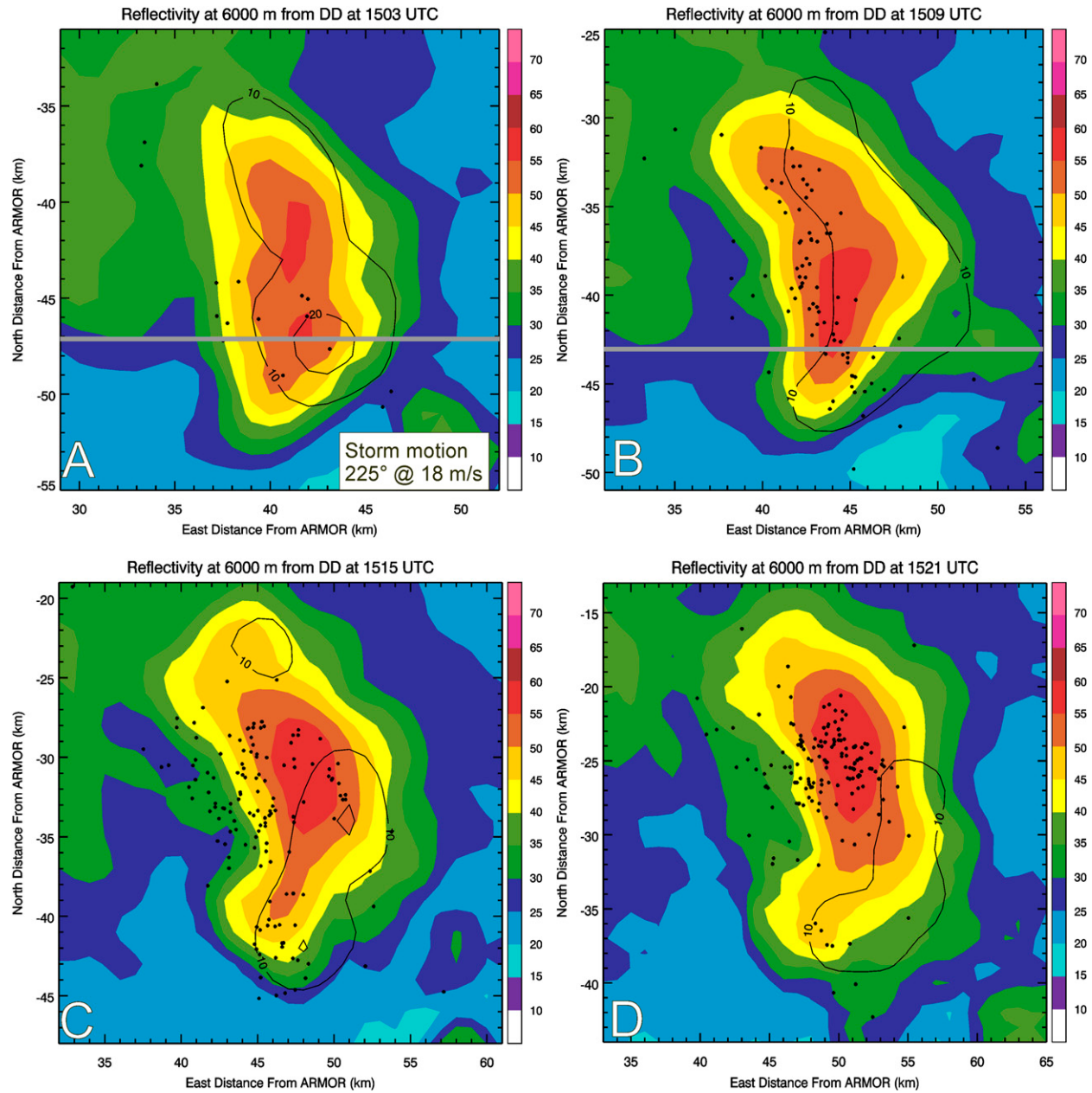


FIG. 14. Reflectivity from ARMOR (dBZ; shaded contours with an interval of 5 dB), vertical velocity (m s^{-1} ; solid black contours at an interval of 10 m s^{-1} starting at 10 m s^{-1}), and lightning initiation points within 3 min of radar volume start time (black dots) at (a) 1503, (b) 1509, (c) 1515, and (d) 1521 UTC at 6 km ARL. Gray lines represent cross-sectional locations taken at $Y = -47 \text{ km}$ (1503 UTC) and $Y = -43 \text{ km}$ (1509 UTC) north of ARMOR in Fig. 18.

2.13 and 2.47, respectively. Prior to both of these jumps, increases in graupel volume, graupel mass, and 10 and 15 m s^{-1} updraft volume occur (Fig. 15; Tables 1 and 2). In fact, the lightning jump at 1528 UTC is in association with decreases in 55 (35)-dBZ reflectivity isosurface height from 6 (10) to 4 (9) km. The 55 (35)-dBZ isosurface height's secondary vertical ascents from 4 (10) to 6 (11) km occur prior to the lightning jump at 1542 UTC

and a 15-mm increase in MESH just prior to 1550 UTC. This growth is followed by a period of high winds and 4.4-cm hail beginning around 1555 UTC (Fig. 16).

The final lightning jump and period of consecutive positive sigma levels (i.e., continuously increasing total flash rates) between 1554 and 1600 UTC occurs as the storm is reaching its peak intensity. Total flash rates are now on the order of $80 \text{ flashes min}^{-1}$. Graupel volume,

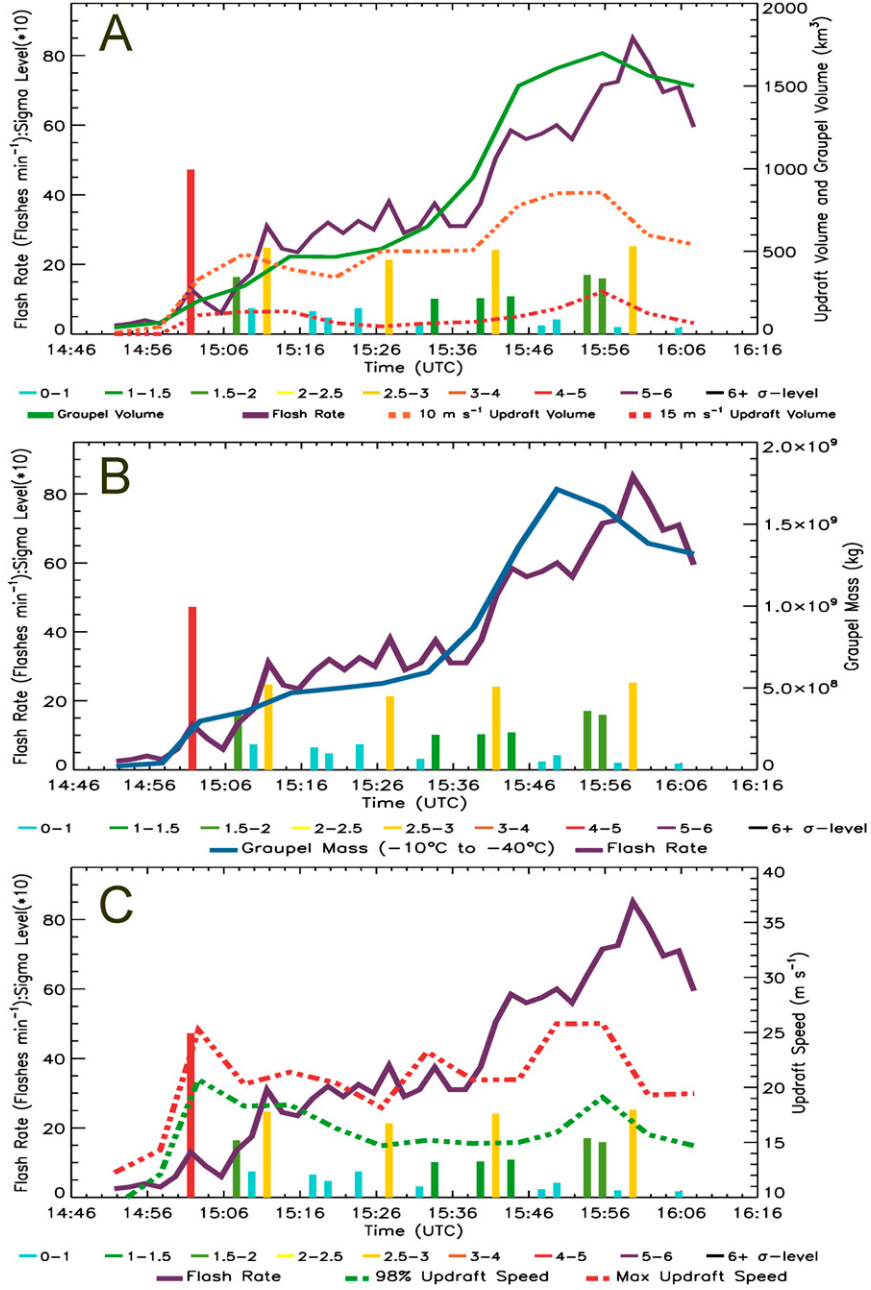


FIG. 15. As in Fig. 3, but for a severe QLCS on 12 Mar 2010 in north-central Alabama.

graupel mass, and 10 and 15 m s⁻¹ updraft volumes all peak between 1550 and 1600 UTC, and the updraft volume begins decreasing by the time of the fifth lightning jump at 1600 UTC (Fig. 15; Tables 1 and 2). The 55-dBZ height reaches its maximum of 7 km and a 65-dBZ core emerges between 3 and 5 km by 1558 UTC (Fig. 16a). MESH once again rapidly increases in magnitude from 40 to 65 mm between 1556 and 1558 UTC in response to the emergence of the 65-dBZ contour (Fig. 16b). Golf ball-sized hail is once again reported at

about 1624 UTC in association with a decrease in height of the 55-dBZ core, and no other lightning jumps are observed during the remainder of the storm's lifetime within the multi-Doppler lobes.

Analysis of mean flash footprint size shows a rapid decrease in mean and median flash size during the period of initial intensification (Fig. 17). Between 1502 and 1506 UTC the average mean and median flash areas are 128 and 127 km², respectively. The maximum flash size is 367 km² (not shown) and is associated with large

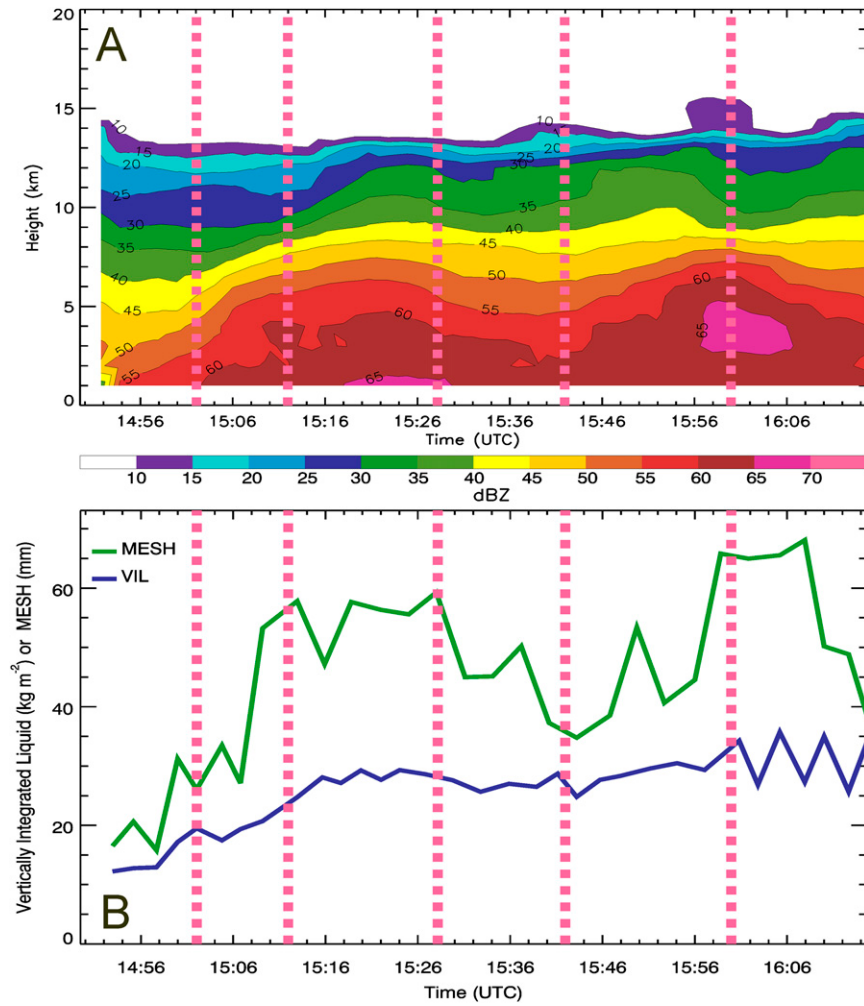


FIG. 16. As in Fig. 4, but for a severe QLCS between 1452 and 1616 UTC 12 Mar 2010 in north-central Alabama. Lightning jumps are at 1502, 1512, 1528, 1542, and 1600 UTC (vertical dashed pink lines).

rearward-propagating flashes into the QLCS's stratiform region that often originate within the forward convective line (e.g., Carey et al. 2005; Ely et al. 2008; Lund et al. 2009). By 1512 UTC, the mean and median flash footprints have fallen to 88 and 77 km², while the peak flash footprint remains large at 306 km² (not shown). Smaller flash sizes are once again located near the peaks in updraft speed, and larger flash sizes are located in the stratiform region (Figs. 18a,c). By 1516 UTC the flash rate begins to increase again, the mean and median flash footprints increase to 110 and 108 km² (Fig. 17), and the maximum flash size is 362 km² (not shown).

However, there are noted differences in the trends of the mean and median flash footprint sizes with time as this storm continues to grow and the trailing stratiform precipitation shield expands. This is clearly noted at 1540 UTC with the fourth lightning jump (Fig. 17).

Notice how as the flash rate increases in magnitude, the mean flash footprint size remains constant around 160 km², while the median footprint size decreases in magnitude from 169 to 93 km² (Fig. 17). During this same period, the maximum flash size nearly doubles from 471 to 908 km² (not shown), and larger flash sizes begin to dominate the mean and eventually the median values as the storm grows and the stratiform region expands. At 1536 UTC, flashes with footprints smaller than 200 km² make up 66% of the 63 flashes between 1536 and 1538 UTC. Ten minutes later, this percentage increases to 70% (86/123), but as the storm expands and intensifies this percentage drops to 54% by 1556 UTC and down to 49% by 1600 UTC (time of the fifth lightning jump). Therefore, the larger size of the storm creates a diversity in flash sizes that masks the flash size–rate relationship.

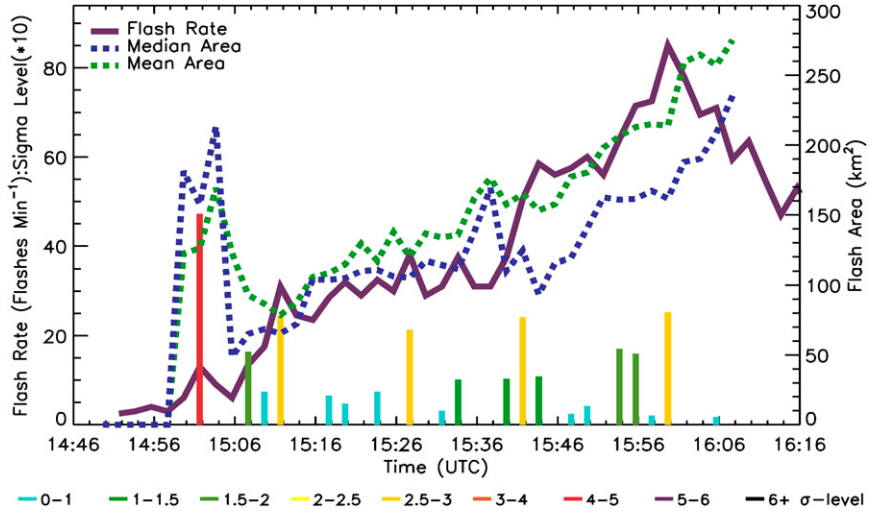


FIG. 17. As in Fig. 5, but for a severe QLCS on 12 Mar 2010 in north-central Alabama.

d. Case 4: Initial supercell development and lightning jump

A unique opportunity to capture the rapid transition from multicellular thunderstorm mode to supercell mode occurs on 10 April 2009 in south-central Tennessee (Figs. 19, 20). Initially this storm lacks a mesocyclone and has a peak total flash rate below 10 flashes min^{-1} . At 1720 UTC the 10 m s^{-1} updraft volume is at 143 km^3 , and the updraft volume greater than 15 m s^{-1} is at 76 km^3 (Fig. 21a). Graupel mass is initially at $2.56 \times 10^8 \text{ kg}$ (Fig. 21b). Peak updraft speed is 27.5 m s^{-1} at 1720 UTC (Fig. 21c). Between 1720 and 1728 UTC, growth of the updraft, graupel volume, graupel mass, and flash rate rapidly occurs. The 10 m s^{-1} updraft volume increases from 143 to 270 km^3 , the 15 m s^{-1} updraft volume doubles to 156 km^3 , and the graupel mass doubles to $5.13 \times 10^8 \text{ kg}$ (Figs. 21a,b; Tables 1 and 2). The maximum and 98th percentile updraft speeds increase as well from 27.5 and 21.2 m s^{-1} to 49.2 and 38.1 m s^{-1} , respectively, between 1720 and 1728 UTC (Fig. 21c). The total flash rate jumps from $8 \text{ flashes min}^{-1}$ at 1724 UTC to $43 \text{ flashes min}^{-1}$ by 1730 UTC (Fig. 21). Two consecutive lightning jumps are observed at 1728 and 1730 UTC with sigma levels of 7.67 and 5.43, respectively.

An increase in intensity metrics for this storm is also readily apparent during this time period between 1720 and 1733 UTC (Fig. 22). The height of the 55-dBZ reflectivity isosurface rises nearly 4 km between 1720 and 1733 UTC (Fig. 22a). Furthermore, there is an increase in the magnitude of the azimuthal shear below 4 km with this storm at the time of the jump (Fig. 22b), and in the next radar volume after the lightning jump a mesocyclone is identified at 1731 UTC (Stough et al. 2015). This

transition to supercellular structure is reinforced by the development of the hook echo by 1739 UTC (Fig. 19d). While no tornado is observed with this storm, the development of low-level rotation and the presence of a mesocyclone in conjunction with the lightning jumps indicates increased potential for severe weather (e.g., Stumpf et al. 1998). Other studies have observed lightning jumps preceding the development of mesocyclones within supercellular environments (e.g., Bruning et al. 2010; Calhoun et al. 2013; Stano et al. 2014; Stough et al. 2015). Finally, there is a distinct upward trend in MESH from 30 to just over 55 mm between 1724 and 1740 UTC (Fig. 22c). At 1746 UTC, 4.4-cm hail fell in Lewisburg, Tennessee.

Mean and median flash footprint sizes drop from 175 and 125 km^2 to 47 and 25 km^2 , respectively, between 1716 and 1730 UTC (Fig. 23). Vertical cross sections of mean flash footprint size at 1720 and 1739 UTC demonstrate that smaller flash footprints are located close to the maximum updraft (Fig. 24). Figure 24 also shows that prior to intensification, smaller flash sizes are confined to a narrow region of the storm just downwind of the updraft location (Figs. 24a,b). After the lightning jump at 1728 UTC, the volume in which flash footprint sizes are smaller than 50 km^2 increased in size as the flash rate increased. Figures 24c and 24d highlight the collocation of the smaller mean flash footprint sizes and the location of the storm's updraft and BWER.

4. Discussion

One of the first takeaways from this study is that both the lightning jump occurrence and the flash rate need to be considered for lightning jump applications to severe

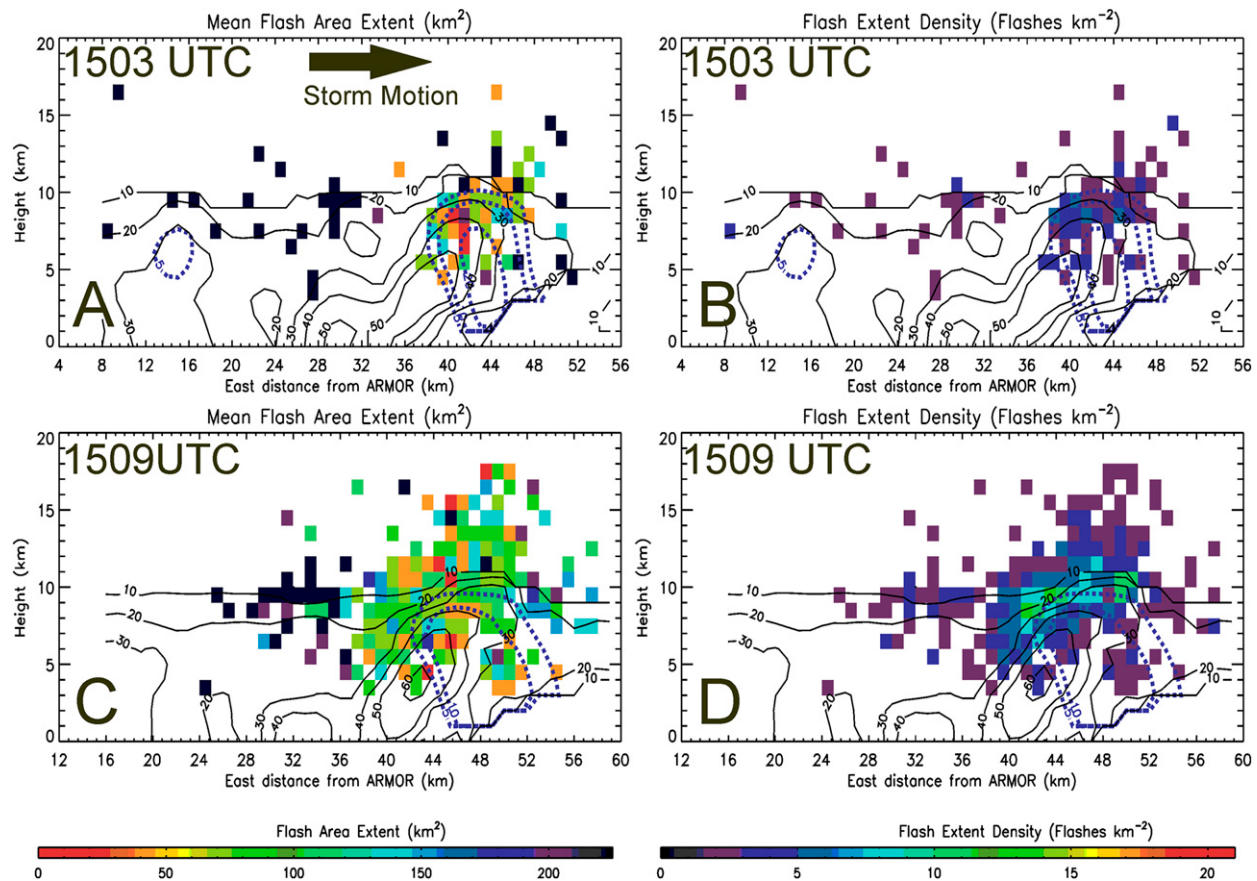


FIG. 18. Vertical cross sections of (a),(c) mean flash footprint and (b),(d) flash extent density leading up to a lightning jump in a bowing segment of a QLCS on 12 Mar 2010 in north-central Alabama. Cross sections were taken at $Y = -47$ km at 1503 UTC (top) and $Y = -43$ km at 1509 UTC (bottom). Reflectivity from ARMOR (dBZ; solid black contours at an interval of 10 dB starting at 10 dBZ) and vertical velocity (m s^{-1} ; blue dashed contours starting at 5 m s^{-1} with an interval of 10 m s^{-1} after 10 m s^{-1}) are overlaid on the mean flash footprint size and flash extent density information. A positive sigma level occurs at 1508 UTC, followed by a lightning jump with a sigma level of 2.47 at 1512 UTC.

storm potential. This is best characterized by the 3 May 2006 multicellular storm. There are three lightning jumps; however, the first jump in comparison with the second and third jumps in this storm highlights why the flash rate needs to be used in conjunction with the lightning jump information. The first jump is small and barely meets the lightning jump flash rate threshold as the total flash rate increased from 5 to 10 flashes min^{-1} . Graupel mass increases by $2.4 \times 10^7 \text{ kg}$ and 10 m s^{-1} updraft (Figs. 8a,b; Tables 1 and 2) and volume remain nearly the same during the 15 min prior to the first lightning jump. Changes in kinematic and microphysical properties were larger with these latter two jumps. Here, the total flash rate increases from 3 to 13 flashes min^{-1} at 2142 UTC and continues to increase up to 29 flashes min^{-1} by 2148 UTC. During the 15 min prior to these last two jumps, the graupel mass increases by $7 \times 10^7 \text{ kg}$ (nearly triple the increase in mass prior to the first time) and

the 10 m s^{-1} updraft volume increases by 62 km^3 (Figs. 8a, b; Tables 1 and 2). Thus, when used in combination, the lightning jump and total flash rate currently provide the optimal configuration for thunderstorm monitoring using lightning data. The lightning jump provides the early indication that rapid intensification is ongoing, while the flash rate provides information relating to the size and intensity of the storm.

Similarly, one particular jump period in Tables 1 and 2 that stands out in this dataset is the fifth jump on 12 March 2010. The kinematic attributes for the storm during this period of time do not fit the model shown in each of the previous examples. Here, the 10 m s^{-1} updraft volume decreases in magnitude during the 15 min prior to this final lightning jump. However, at the time of the decrease, both graupel mass and 10 m s^{-1} updraft volume are at their largest magnitudes for the storm. Also, the majority of the graupel mass increase at this

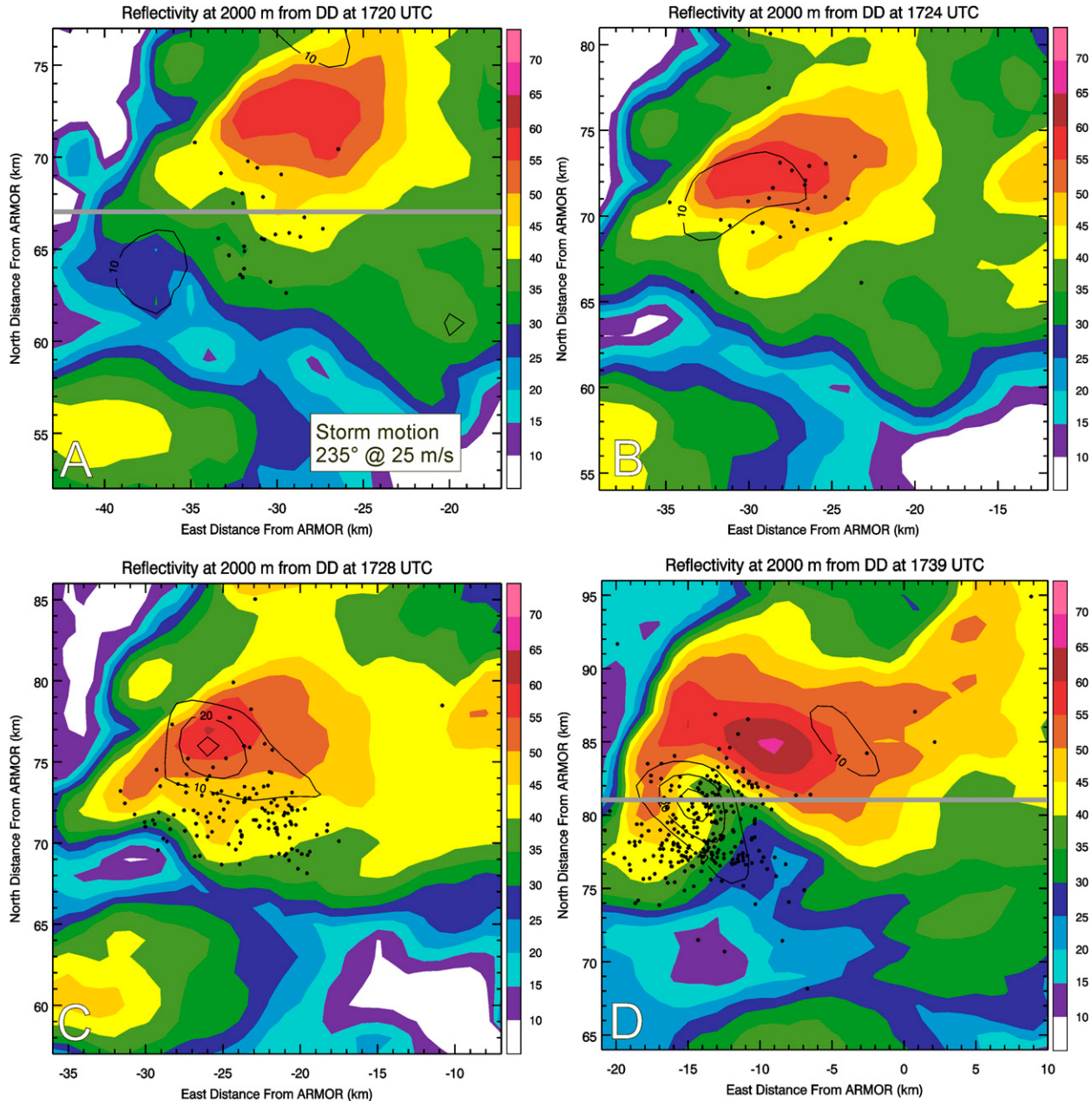


FIG. 19. CAPPIs at 2 km ARL on 10 Apr 2009 for a supercell storm in south-central Tennessee. Reflectivity is from ARMOR (dBZ); shaded contours with an interval of 5 dB, vertical velocity (m s^{-1} ; solid black contours at an interval of 10 m s^{-1} starting at 10 m s^{-1}), and lightning initiation points within 3 min of the radar volume start time (black dots) at (a) 1720, (b) 1724, (c) 1728, and (d) 1739 UTC. Gray lines represent cross-sectional locations at $Y = 67 \text{ km}$ north of ARMOR (1720 UTC) and $Y = 81 \text{ km}$ north of ARMOR (1739 UTC) in Fig. 24.

time is below the layer from -10° to -40°C at the time of this jump. Graupel mass between 0° and -10°C increases by $9.3 \times 10^8 \text{ kg}$ during this period. While much of this increase in graupel mass may be due to graupel mass fallout from -10° to -40°C , over 35% ($3.7 \times 10^8 \text{ kg}$) of the increase in graupel mass in this layer is found in regions where updrafts are located. Furthermore, the

authors can reasonably speculate on the potential role for secondary ice generation processes leading up to the final jump (e.g., Hallett and Mossop 1974; Mansell et al. 2010). Secondary ice generation processes are the result of the splintering of graupel and fracturing of freezing drops between -3° and -8°C near or within a thunderstorm updraft. Thus, evidence of graupel mass growth

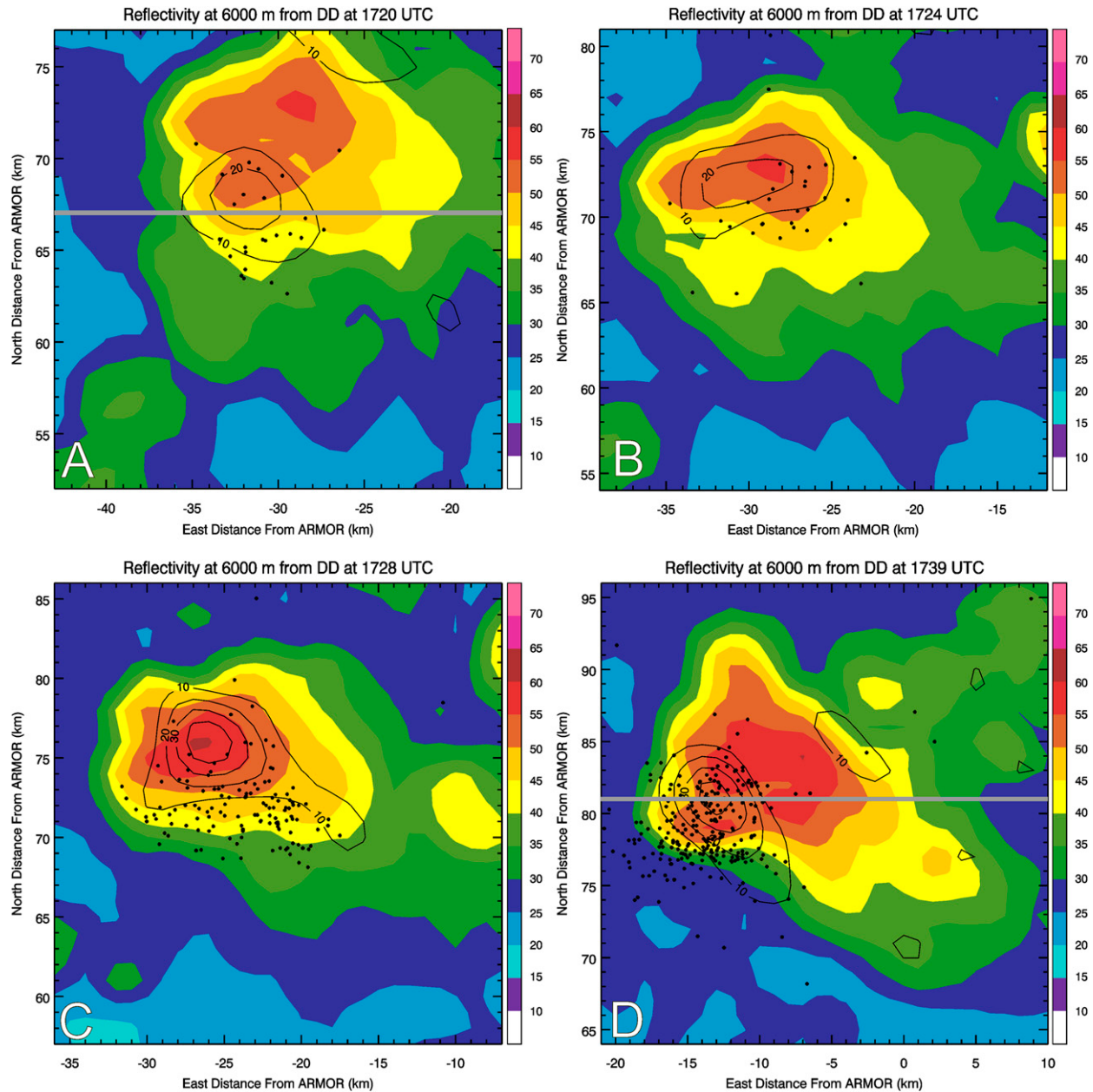


FIG. 20. As in Fig. 19, but for CAPPIs at 6 km ARL. Gray lines denote the location of cross sections in Fig. 24.

within the updraft of the storm between 0° and -10°C provides a reasonable physical basis for the presence of secondary ice production by which an enhancement in electrification can be realized in this storm.

Thus, not all jumps have the same characteristics, and it is important to examine the jump, the duration of the jump (i.e., in this case two vs eight consecutive minutes with positive sigma levels), and the resultant flash rate for optimal use in a warning environment. These observations are also supported by the recent work of Chronis et al. (2015). Chronis et al. (2015) demonstrate

that storms with lightning jumps that contained higher-magnitude flash rates and sigma levels correspond to storms that eventually produce higher MESH values and last longer in time.

Table 1 highlights changes in graupel mass of each storm prior to individual lightning jumps with sigma levels that are 2 and higher and the maximum flash rate increase in the 11 June storm. The consistent observation across the board for each storm is an increase in graupel mass as the total flash rate increases. The change in mixed-phase graupel mass is at least $7 \times 10^7 \text{ kg}$ and/or

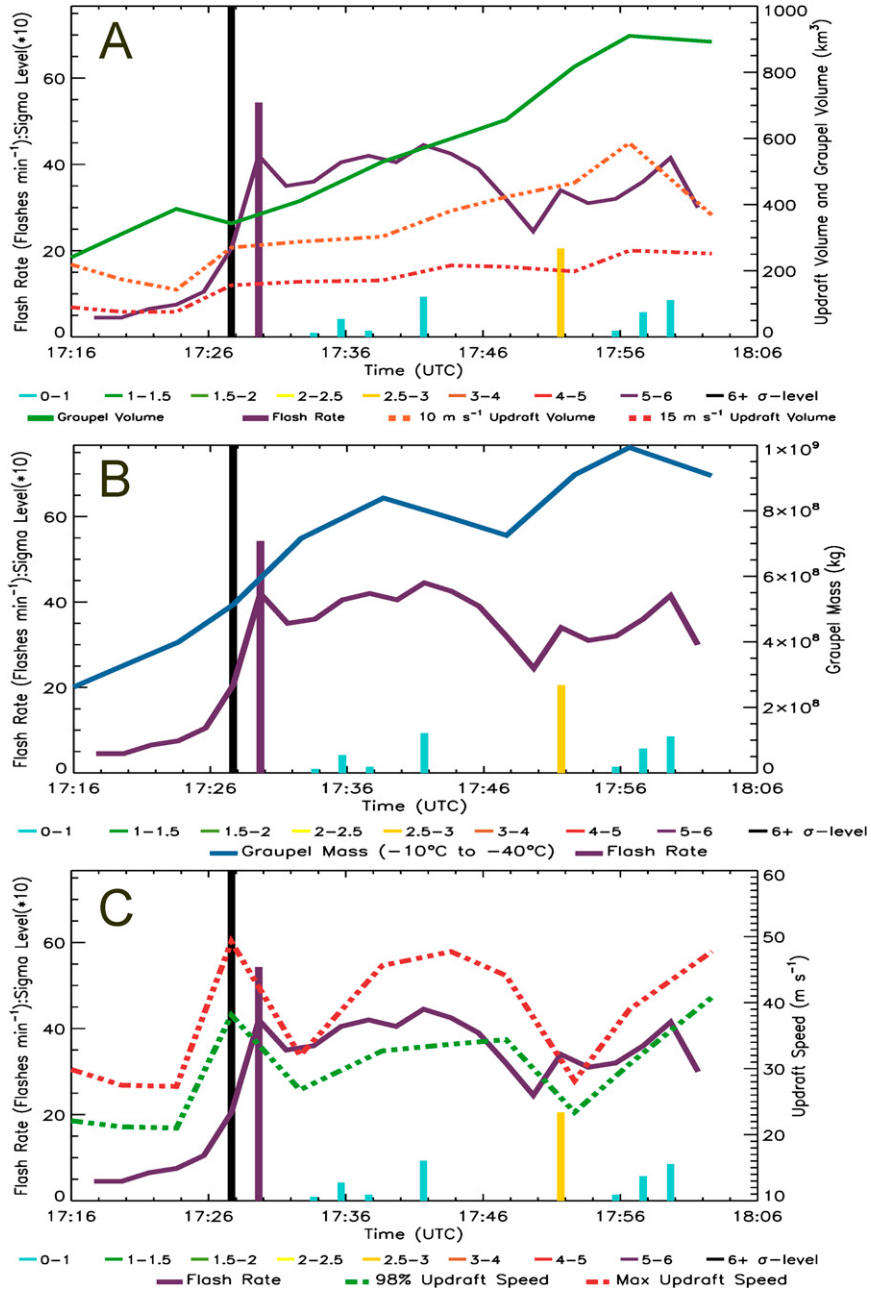


FIG. 21. As in Fig. 3, but for a developing supercell on 10 Apr 2009 in south-central Tennessee.

ice mass greater than 10^8 kg was already in place in the lightning jumps that precede severe weather occurrence. In the weakest case, the change in graupel mass is only on the order of $2.3 \times 10^7 \text{ kg}$, with a resultant graupel mass not exceeding $4.4 \times 10^7 \text{ kg}$.

Kinematic characteristics are summarized in Table 2 for all 12 periods of interest. The first observation that corroborates previous studies is that larger updraft volumes support higher flash rates (e.g., Lang and Rutledge 2002; Kuhlman et al. 2006; Deierling and

Petersen 2008; Calhoun et al. 2013). This result is especially apparent when comparing 10 m s^{-1} updraft volumes. All but two increases in total flash rate are preceded by increases in the 10 m s^{-1} updraft volume. The change in updraft volume with the second and third lightning jumps on 3 May 2006 is likely underestimated because a substantial period of the storms lifetime was omitted because it approached the edge of the 30° beam-crossing angle in the ARMOR-KHTX multi-Doppler lobe.

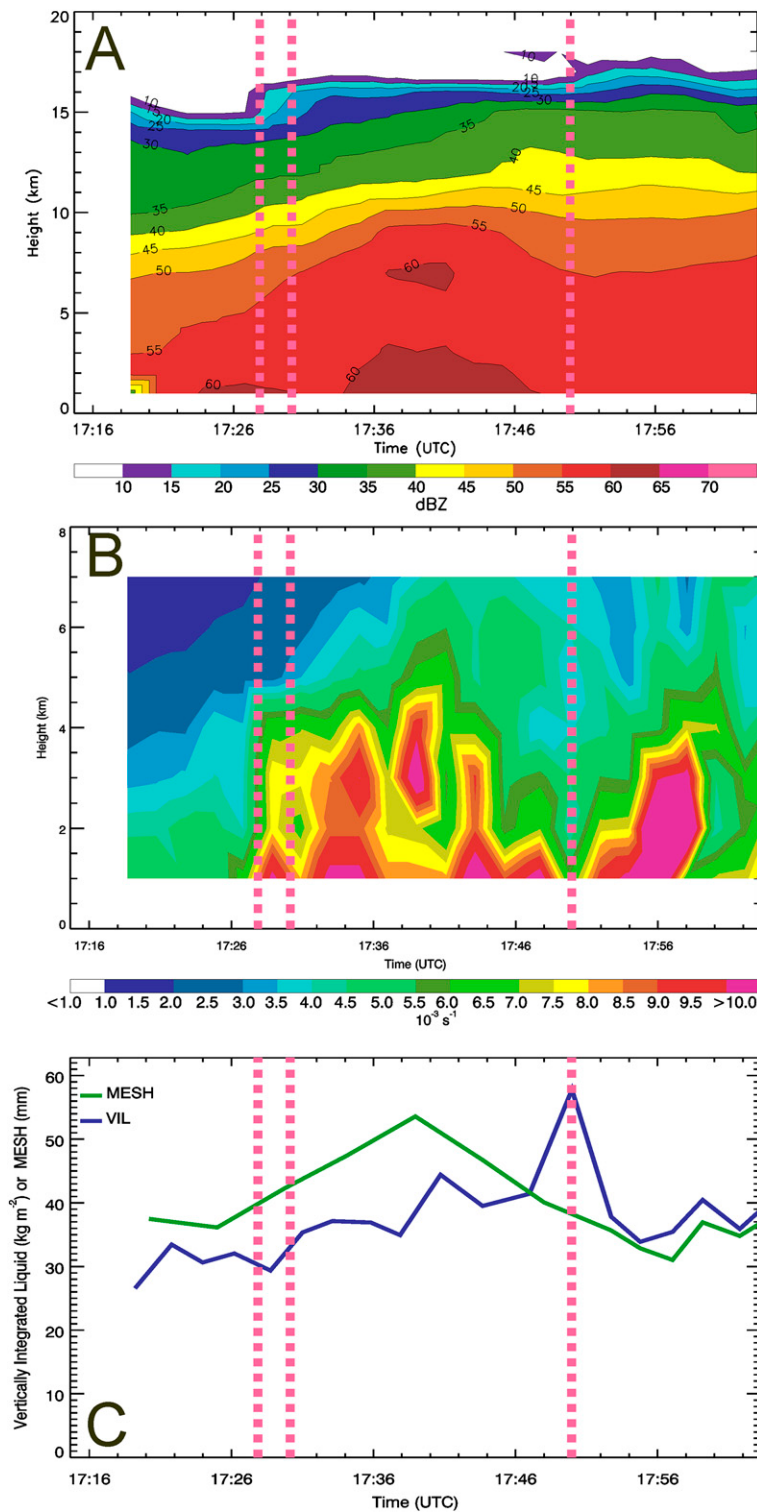


FIG. 22. Time–height of (a) max reflectivity (dBZ; shaded contours with an interval of 5 dB) and (b) azimuthal shear (s^{-1} ; shaded contours at an interval of 10^{-3} s^{-1} between 10^{-3} and 10^{-2} s^{-1}). (c) The time trend of MESH (mm; green line) and VIL (kg m^{-2} ; blue line) between 1718 and 1806 UTC 10 Apr 2009 in south-central Tennessee from KHTX. The lightning jump times were 1728, 1730, and 1750 UTC (vertical dashed pink lines).

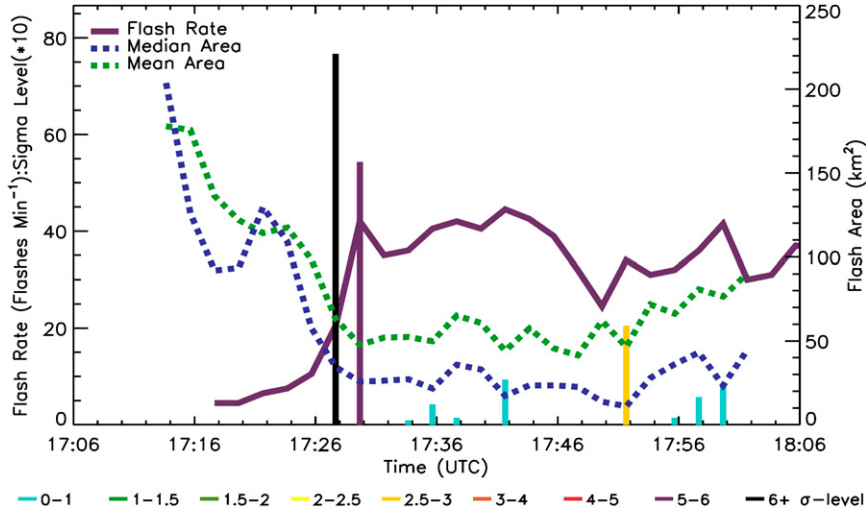


FIG. 23. As in Fig. 5, but for a developing supercell on 10 Apr 2009 in south-central Tennessee.

Maximum and 98th percentile updraft speed increased in 8 of 12 instances prior to lightning jump occurrence (Table 2). However, peak updraft speed is found not to be as well correlated to the total flash rate when compared to the 10 m s^{-1} updraft volume–total flash rate relationship over the entire history of each thunderstorm using Spearman's rank correlation (Table 3). Higher positive correlation coefficients and lower standard error values are found for the 10 m s^{-1} updraft volume–total flash rate relationship versus the peak updraft speed–total flash rate relationship, indicating that there is better agreement between the updraft size and total flash rate versus the peak updraft speed and total flash rate over the lifetime of these thunderstorms. Thus, even though an increase in maximum updraft speed corresponds well with the lightning jumps in these events on shorter time scales, the maximum updraft is not necessarily well correlated to the total flash rate over the entire lifetime of a thunderstorm. This observation of poorer correlation between peak updraft speed and total flash rate versus the correlation between updraft volume and total flash rate over an entire storm's history supports the findings of Lang and Rutledge (2002), Kuhlman et al. (2006), and Deierling and Petersen (2008).

The inverse relationship between flash rate and flash size is observed near the times of most lightning jumps. However, once storms have matured, this relationship can break down at the storm scale with the development of larger flashes within anvils or stratiform regions (e.g., 1556–1606 UTC 12 March 2010; Fig. 17). When flash sizes can spatially be resolved through lightning measurements, locations of flash size minima highlighted updraft locations. Furthermore, modulation of flash size in time and space can also be a good indicator of local

modulation to updraft strength. Importantly, many of the mean and median footprint sizes in each of the trends are less than 64 km^2 , so application of this flash size and flash rate inverse relationship to lightning data from instruments like the Geostationary Lightning Mapper (GLM; $8 \text{ km} \times 8 \text{ km}$ footprint at nadir) may be challenging because of the coarseness of the measurements.

5. Conclusions

Kinematic, microphysical, and flash characteristics were examined for four thunderstorms in northern Alabama and south-central Tennessee during rapid increases in total lightning. The organization and intensity of these four thunderstorms range from an ordinary thunderstorm to a well-organized and long-lived supercell. Three of the four thunderstorms that are examined contained at least one lightning jump. The fourth storm from 11 June 2012 did not produce a jump and is analyzed at the time of its greatest flash rate increase.

These results show that a combination of microphysical and kinematic quantities is necessary for the total flash rate to rapidly increase in an intensifying thunderstorm. The following observations are made connecting the kinematic and microphysical thunderstorm characteristics to lightning jumps:

- Lightning jumps are observed in conjunction with growth of the 10 m s^{-1} updraft volume and graupel mass between -10° and -40°C .
- Peak and 98th percentile updraft speeds are observed to increase in magnitude in 8 of the 12 lightning jumps and peak flash rate increases examined here; however, over the entire lifetime of each storm, peak updraft

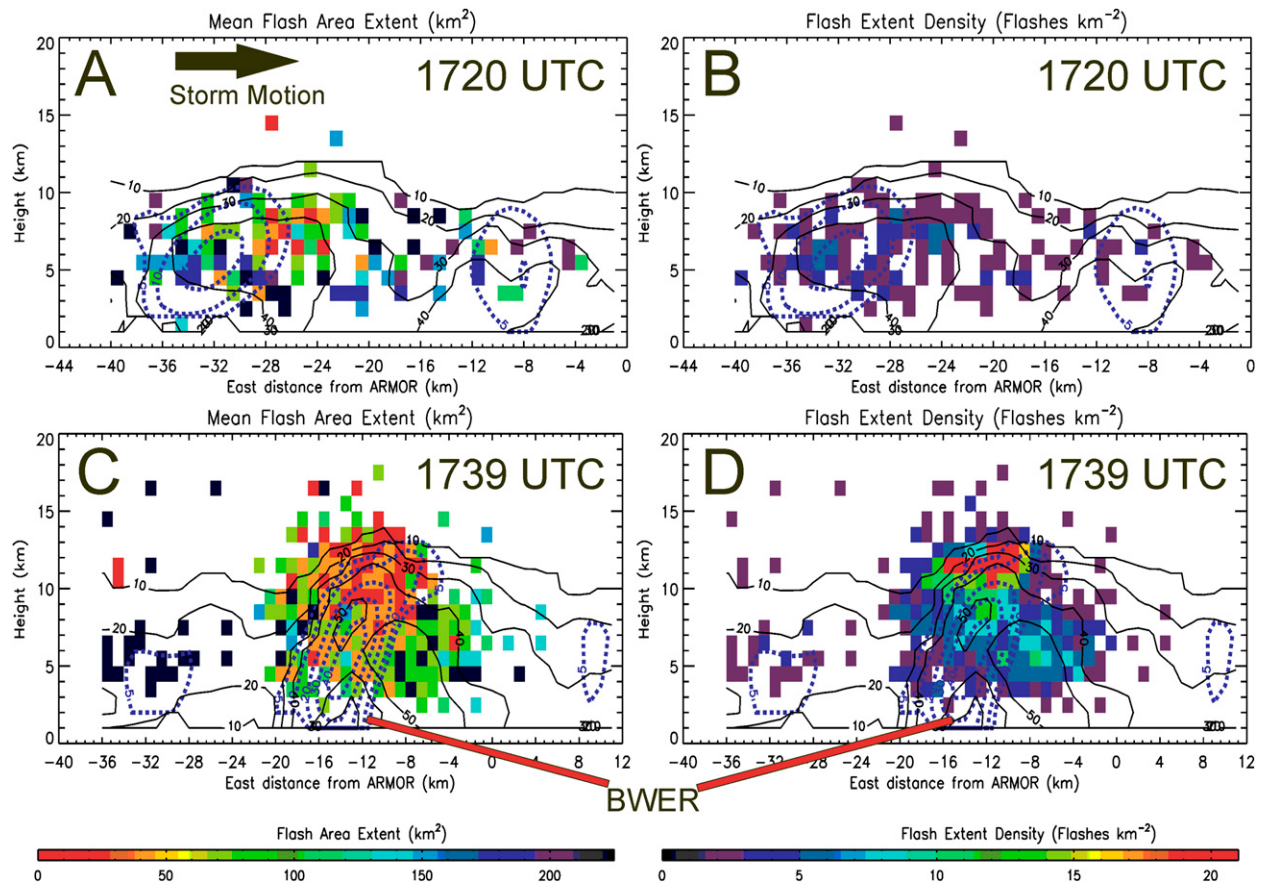


FIG. 24. Vertical cross sections of (a),(c) mean flash footprint and (b),(d) flash extent density before and after a lightning jump for a developing supercell on 10 Apr 2009 in south-central Tennessee. Cross sections were taken at $Y = 67$ km at 1720 UTC (top) and $Y = 74$ km at 1739 UTC (bottom). Lightning jump time was 1728 UTC. Reflectivity from ARMOR (dBZ; solid black contours with an interval of 10 dB) and vertical velocity (m s^{-1} ; blue dashed contours starting at 5 m s^{-1} with an interval of 10 m s^{-1} after 10 m s^{-1}) are overlaid on the mean flash footprint size and flash extent density information.

speed is not well correlated with total flash rate. This demonstration of poorer correlation between the updraft speed and total flash rate versus the updraft volume and total flash rate over the lifetime of thunderstorms is similar to the findings of previous work.

- Decreases in mean and median flash footprints during increases in the total lightning flash rate are observed in all four thunderstorms during development stages within the most intense storms.

- The smallest flash sizes in each thunderstorm are located near the most intense updrafts during these growth phases, as postulated by Bruning and MacGorman (2013).
- The combination of both the sigma level and the total flash rate are important when using total lightning observations to assess storm intensification.

Most importantly, these results serve as conceptual models for future lightning and lightning jump applications to assess severe weather potential. The lightning and lightning jump provide the forecaster information

on the state of a thunderstorm's updraft, which can be used to make timely warning decisions in conjunction with other readily available observations (e.g., radar, satellite, and environmental information). Current research by Schultz (2015) quantifies kinematic and microphysical changes for all flash rate increases in a large number of storms to work in concert with the examples presented in this paper.

TABLE 3. Spearman's correlation R and standard error analysis σ_{SE} between max updraft speed w_{Max} and 10 m s^{-1} updraft volume w_{10} to total flash rate for each thunderstorm's entire lifetime.

Event	w_{Max}		w_{10}	
	R	σ_{SE}	R	σ_{SE}
11 Jun 2012	0.584	0.036	0.802	9×10^{-4}
3 May 2006	0.209	0.561	0.543	0.105
12 Mar 2010	0.332	0.246	0.876	4×10^{-5}
10 Apr 2009	0.397	0.226	0.744	0.008

Acknowledgments. The authors would like to acknowledge Dr. Steven J. Goodman and NOAA/NASA GOES-R Risk Reduction Research funding for support of this research. CJS would like to acknowledge support from the NASA Pathways Intern Program at Marshall Space Flight Center, namely Julie Clift and Christopher Randall. The authors are thankful for technical support with radar data processing from Lamont Bain, Retha Mecikalski, and Danielle Kozlowski for parts of the 11 June and 10 April events. The authors would like to also acknowledge Dr. Walt Petersen for directing the collection of ARMOR data during his tenure at the Earth System Science Center and NASA MSFC in Huntsville. Furthermore, productive conversations with Themis Chronis, Phil Bitzer, Hugh Christian, and Kristin Calhoun benefited the outcomes of this research. We also gratefully acknowledge the technical support for maintenance of the operational instrumentation, namely Dustin Phillips, Patrick Gatlin, and Chris Phillips for the maintenance of ARMOR, and Jeff Bailey for the continued maintenance of the North Alabama Lightning Mapping Array. Finally, we thank Dr. Eric Bruning and two anonymous reviewers for thorough and constructive reviews that improved this article.

REFERENCES

- Armijo, L., 1969: A theory for the determination of wind and precipitation velocities with Doppler radars. *J. Atmos. Sci.*, **26**, 570–573, doi:10.1175/1520-0469(1969)026<0570:ATFTDO>2.0.CO;2.
- Bain, A. L., 2013: Polarimetric Doppler radar and electrical observations of deep moist convection across northern Alabama during the Deep Convective Clouds and Chemistry Experiment. M.S. thesis, Dept. of Atmospheric Science, University of Alabama in Huntsville, 148 pp. [Available online at http://armor.nsstc.uah.edu/publications/Bain_thesis.pdf.]
- Barth, M., and Coauthors, 2014: The Deep Convective Clouds and Chemistry (DC3) field campaign. *Bull. Amer. Meteor. Soc.*, **96**, 1281–1309, doi:10.1175/BAMS-D-13-00290.1
- Barthe, C., W. Deierling, and M. C. Barth, 2010: Estimation of total lightning from various storm parameters: A cloud-resolving model study. *J. Geophys. Res.*, **115**, D24202, doi:10.1029/2010JD014405.
- Boccippio, D. J., 2002: Lightning scaling relations revisited. *J. Atmos. Sci.*, **59**, 1086–1104, doi:10.1175/1520-0469(2002)059<1086:LSR>2.0.CO;2.
- Brandes, E. A., 1977: Flow in severe thunderstorms observed by dual-Doppler radar. *Mon. Wea. Rev.*, **105**, 113–120, doi:10.1175/1520-0493(1977)105<0113:FISTOB>2.0.CO;2.
- Bringi, V. N., K. R. Knupp, A. Detwiler, L. Liu, I. J. Taylor, and R. A. Black, 1997: Evolution of a Florida thunderstorm during the Convection and Precipitation/Electrification Experiment: The case of 9 August 1991. *Mon. Wea. Rev.*, **125**, 2131–2160, doi:10.1175/1520-0493(1997)125<2131:EOAFTD>2.0.CO;2.
- , T. D. Keenan, and V. Chandrasekar, 2001: Correcting C-band radar reflectivity and differential reflectivity data for rain attenuation: A self-consistent method with constraints. *IEEE Trans. Geosci. Remote Sens.*, **39**, 1906–1915, doi:10.1109/36.951081.
- Bruning, E. C., and D. M. MacGorman, 2013: Theory and observations of controls on lightning flash spectra. *J. Atmos. Sci.*, **70**, 4012–4029, doi:10.1175/JAS-D-12-0289.1.
- , W. D. Rust, D. R. MacGorman, M. I. Biggerstaff, and T. J. Schurr, 2010: Formation of charge structures in a supercell. *Mon. Wea. Rev.*, **138**, 3740–3761, doi:10.1175/2010MWR3160.1.
- Calhoun, K. M., 2015: Forecaster use of total lightning data for short-term forecasts and warnings in the Hazardous Weather Testbed. *Proc. Seventh Conf. on Meteorological Applications of Lightning Data*, Phoenix, AZ, Amer. Meteor. Soc., 3.5. [Available online at <https://ams.confex.com/ams/95Annual/webprogram/Paper268336.html>.]
- , D. R. MacGorman, C. L. Ziegler, and M. I. Biggerstaff, 2013: Evolution of lightning activity and storm charge relative to dual-Doppler analysis of a high-precipitation supercell storm. *Mon. Wea. Rev.*, **141**, 2199–2223, doi:10.1175/MWR-D-12-00258.1.
- , T. M. Smith, D. M. Kingfield, J. Gao, and D. J. Stensrud, 2014: Forecaster use and evaluation of real-time 3DVAR analyses during severe thunderstorm and tornado warning operations in the Hazardous Weather Testbed. *Wea. Forecasting*, **29**, 601–613, doi:10.1175/WAF-D-13-00107.1.
- Carey, L. D., and S. A. Rutledge, 1996: A multiparameter radar case study of the microphysical and kinematic evolution of a lightning producing storm. *Meteor. Atmos. Phys.*, **59**, 33–64, doi:10.1007/BF01032000.
- , and —, 2000: On the relationship between precipitation and lightning in tropical island convection: A C-band polarimetric radar study. *Mon. Wea. Rev.*, **128**, 2687–2710, doi:10.1175/1520-0493(2000)128<2687:TRBPAL>2.0.CO;2.
- , M. J. Murphy, T. L. McCormick, and N. W. Demetriades, 2005: Lightning location relative to storm structure in a leading-line trailing stratiform mesoscale convective system. *J. Geophys. Res.*, **110**, D03105, doi:10.1029/2003JD004371.
- Cecil, D. J., S. J. Goodman, D. J. Boccippio, E. J. Zipser, and S. W. Nesbitt, 2005: Three years of TRMM precipitation features. Part I: Radar, radiometric, and lightning characteristics. *Mon. Wea. Rev.*, **133**, 543–566, doi:10.1175/MWR-2876.1.
- Chronis, T., L. D. Carey, C. J. Schultz, E. V. Schultz, K. M. Calhoun, and S. J. Goodman, 2015: Exploring lightning jump characteristics. *Wea. Forecasting*, **30**, 23–37, doi:10.1175/WAF-D-14-00064.1.
- Cintineo, J. L., T. M. Smith, V. Lakshmanan, H. E. Brooks, and K. L. Ortega, 2012: An objective high-resolution hail climatology of the contiguous United States. *Wea. Forecasting*, **27**, 1235–1248, doi:10.1175/WAF-D-11-00151.1.
- Coniglio, M. C., S. F. Corfidi, and J. S. Kain, 2011: Environment and early evolution of the 8 May 2009 derecho-producing convective system. *Mon. Wea. Rev.*, **139**, 1083–1102, doi:10.1175/2010MWR3413.1.
- Crum, T. D., and R. L. Albert, 1993: The WSR-88D and the WSR-88D Operational Support Facility. *Bull. Amer. Meteor. Soc.*, **74**, 1669–1687, doi:10.1175/1520-0477(1993)074<1669:TWATWO>2.0.CO;2.
- Davies-Jones, R. P., 1979: Dual-Doppler radar coverage area as a function of measurement accuracy and spatial resolution. *J. Appl. Meteor.*, **18**, 1229–1233, doi:10.1175/1520-0450-18.9.1229.
- Deierling, W., and W. A. Petersen, 2008: Total lightning activity as an indicator of updraft characteristics. *J. Geophys. Res.*, **113**, D16210, doi:10.1029/2007JD009598.
- , —, J. Latham, S. Ellis, and H. J. Christian, 2008: The relationship between lightning activity and ice fluxes in thunderstorms. *J. Geophys. Res.*, **113**, D15210, doi:10.1029/2007JD009700.

- Dixon, M., and G. Wiener, 1993: TITAN: Thunderstorm Identification, Tracking, Analysis, and Nowcasting—A radar-based methodology. *J. Atmos. Oceanic Technol.*, **10**, 785–797, doi:[10.1175/1520-0426\(1993\)010<0785:TTITAA>2.0.CO;2](https://doi.org/10.1175/1520-0426(1993)010<0785:TTITAA>2.0.CO;2).
- Dye, J. E., and Coauthors, 1986: Early electrification and precipitation development in a small, isolated Montana cumulonimbus. *J. Geophys. Res.*, **91**, 1231–1247, doi:[10.1029/JD091iD01p01231](https://doi.org/10.1029/JD091iD01p01231).
- , W. P. Winn, J. J. Jones, and D. W. Breed, 1989: The electrification of New Mexico thunderstorms. 1. Relationship between precipitation development and the onset of electrification. *J. Geophys. Res.*, **94**, 8643–8656, doi:[10.1029/JD094iD06p08643](https://doi.org/10.1029/JD094iD06p08643).
- Ely, B. L., R. E. Orville, L. D. Carey, and C. L. Hodapp, 2008: Evolution of the total lightning structure in a leading-line, trailing-stratiform mesoscale convective system over Houston, Texas. *J. Geophys. Res.*, **113**, D08114, doi:[10.1029/2007JD008445](https://doi.org/10.1029/2007JD008445).
- Gatlin, P. N., and S. J. Goodman, 2010: A total lightning trending algorithm to identify severe thunderstorms. *J. Atmos. Oceanic Technol.*, **27**, 3–22, doi:[10.1175/2009JTECHA1286.1](https://doi.org/10.1175/2009JTECHA1286.1).
- Goodman, S. J., D. E. Buechler, P. D. Wright, and W. D. Rust, 1988: Lightning and precipitation history of a microburst-producing storm. *Geophys. Res. Lett.*, **15**, 1185–1188, doi:[10.1029/GL015i011p01185](https://doi.org/10.1029/GL015i011p01185).
- , and Coauthors, 2005: The North Alabama Lightning Mapping Array: Recent severe storm observations and future prospects. *Atmos. Res.*, **76**, 423–437, doi:[10.1016/j.atmosres.2004.11.035](https://doi.org/10.1016/j.atmosres.2004.11.035).
- Greene, D. R., and R. A. Clarke, 1972: Vertically integrated liquid water—A new analysis tool. *Mon. Wea. Rev.*, **100**, 548–552, doi:[10.1175/1520-0493\(1972\)100<0548:VILWNA>2.3.CO;2](https://doi.org/10.1175/1520-0493(1972)100<0548:VILWNA>2.3.CO;2).
- Hallett, J., and S. C. Mossop, 1974: Production of secondary ice particles during the riming process. *Nature*, **249**, 26–28, doi:[10.1038/249026a0](https://doi.org/10.1038/249026a0).
- Heymsfield, A. J., and M. R. Hjelmfelt, 1984: Processes of hydrometeor development in Oklahoma convective clouds. *J. Atmos. Sci.*, **41**, 2811–2835, doi:[10.1175/1520-0469\(1984\)041<2811:POHDIO>2.0.CO;2](https://doi.org/10.1175/1520-0469(1984)041<2811:POHDIO>2.0.CO;2).
- , and K. M. Miller, 1988: Water vapor and ice mass transported into the anvils of CCOPE thunderstorms: Comparison with storm influx and rainout. *J. Atmos. Sci.*, **45**, 3501–3514, doi:[10.1175/1520-0469\(1988\)045<3501:WVAIMT>2.0.CO;2](https://doi.org/10.1175/1520-0469(1988)045<3501:WVAIMT>2.0.CO;2).
- Houze, R. A., Jr., 1989: Observed structure of mesoscale convective systems and implications for large-scale heating. *Quart. J. Roy. Meteor. Soc.*, **115**, 425–461, doi:[10.1002/qj.49711548702](https://doi.org/10.1002/qj.49711548702).
- Johnson, E. V., 2009: Behavior of lightning and updrafts for severe and non severe thunderstorms in northern Alabama. M.S. thesis, Dept. of Atmospheric Science, University of Alabama in Huntsville, 70 pp. [Available online at <http://vortex.nsstc.uah.edu/~johnson/docs/elisethesis.pdf>.]
- Knupp, K. R., and Coauthors, 2014: Meteorological overview of the devastating 27 April 2011 tornado outbreak. *Bull. Amer. Meteor. Soc.*, **95**, 1041–1062, doi:[10.1175/BAMS-D-11-00229.1](https://doi.org/10.1175/BAMS-D-11-00229.1).
- Koshak, W. J., and Coauthors, 2004: North Alabama Lightning Mapping Array (LMA): VHF source retrieval algorithm and error analysis. *J. Atmos. Oceanic Technol.*, **21**, 543–558, doi:[10.1175/1520-0426\(2004\)021<0543:NALMAL>2.0.CO;2](https://doi.org/10.1175/1520-0426(2004)021<0543:NALMAL>2.0.CO;2).
- Kuhlman, K. M., C. L. Ziegler, E. R. Mansell, D. R. MacGorman, and J. M. Straka, 2006: Numerically simulated electrification and lightning of the 29 June 2000 STEPS supercell storm. *Mon. Wea. Rev.*, **134**, 2734–2757, doi:[10.1175/MWR3217.1](https://doi.org/10.1175/MWR3217.1).
- Lakshmanan, V., T. Smith, K. Hondl, G. J. Stumpf, and A. Witt, 2006: A real-time, three-dimensional, rapidly updating, heterogeneous radar merger technique for reflectivity, velocity, and derived products. *Wea. Forecasting*, **21**, 802–823, doi:[10.1175/WAF942.1](https://doi.org/10.1175/WAF942.1).
- Lang, T. J., and S. A. Rutledge, 2002: Relationships between convective storm kinematics, precipitation, and lightning. *Mon. Wea. Rev.*, **130**, 2492–2506, doi:[10.1175/1520-0493\(2002\)130<2492:RBCSKP>2.0.CO;2](https://doi.org/10.1175/1520-0493(2002)130<2492:RBCSKP>2.0.CO;2).
- Lund, N. R., D. R. MacGorman, T. J. Schuur, M. I. Biggerstaff, and W. D. Rust, 2009: Relationships between lightning location and polarimetric radar signatures in a small mesoscale convective system. *Mon. Wea. Rev.*, **137**, 4151–4170, doi:[10.1175/2009MWR2860.1](https://doi.org/10.1175/2009MWR2860.1).
- MacGorman, D. R., D. W. Burgess, V. Mazur, W. D. Rust, W. L. Taylor, and B. C. Johnson, 1989: Lightning rates relative to tornadic storm evolution on 22 May 1981. *J. Atmos. Sci.*, **46**, 221–250, doi:[10.1175/1520-0469\(1989\)046<0221:LRRTTS>2.0.CO;2](https://doi.org/10.1175/1520-0469(1989)046<0221:LRRTTS>2.0.CO;2).
- Mansell, E. R., C. L. Ziegler, and E. C. Bruning, 2010: Simulated electrification of a small thunderstorm with two-moment bulk microphysics. *J. Atmos. Sci.*, **67**, 171–194, doi:[10.1175/2009JAS2965.1](https://doi.org/10.1175/2009JAS2965.1).
- Marks, F. D., and R. A. Houze Jr., 1987: Inner core structure of Hurricane Alicia from airborne Doppler radar observations. *J. Atmos. Sci.*, **44**, 1296–1317, doi:[10.1175/1520-0469\(1987\)044<1296:ICSOHA>2.0.CO;2](https://doi.org/10.1175/1520-0469(1987)044<1296:ICSOHA>2.0.CO;2).
- Matejka, T., and D. L. Bartels, 1998: The accuracy of vertical air velocities from Doppler radar data. *Mon. Wea. Rev.*, **126**, 92–117, doi:[10.1175/1520-0493\(1998\)126<0092:TAOVAV>2.0.CO;2](https://doi.org/10.1175/1520-0493(1998)126<0092:TAOVAV>2.0.CO;2).
- McCaul, E. W., S. J. Goodman, K. M. LaCasse, and D. J. Cecil, 2009: Forecasting lightning threat using cloud-resolving model simulations. *Wea. Forecasting*, **24**, 709–729, doi:[10.1175/2008WAF2222152.1](https://doi.org/10.1175/2008WAF2222152.1).
- Metzger, E., and W. A. Nuss, 2013: The relationship between total cloud lightning behavior and radar-derived thunderstorm structure. *Wea. Forecasting*, **28**, 237–253, doi:[10.1175/WAF-D-11-00157.1](https://doi.org/10.1175/WAF-D-11-00157.1).
- Mohr, C. G., L. J. Miller, R. L. Vaughn, and H. W. Frank, 1986: On the merger of mesoscale datasets into a common Cartesian format for efficient and synthetic analysis. *J. Atmos. Oceanic Technol.*, **3**, 143–161, doi:[10.1175/1520-0426\(1986\)003<0143:TMOMDI>2.0.CO;2](https://doi.org/10.1175/1520-0426(1986)003<0143:TMOMDI>2.0.CO;2).
- O'Brien, J. J., 1970: Alternative solutions to the classical vertical velocity problem. *J. Appl. Meteor.*, **9**, 197–203, doi:[10.1175/1520-0450\(1970\)009<0197:ASTTCV>2.0.CO;2](https://doi.org/10.1175/1520-0450(1970)009<0197:ASTTCV>2.0.CO;2).
- Oye, D., and M. Case, 1995: REORDER: A program for gridding radar data. Installation and user manual for the UNIX version. NCAR Atmospheric Technology Division, 19 pp.
- , C. Mueller, and S. Smith, 1995: Software for radar translation, visualization, editing and interpolation. Preprints, *27th Conf. on Radar Meteorology*, Vail, CO, Amer. Meteor. Soc., 359–361.
- Ray, P. S., C. L. Ziegler, W. Bumgarner, and R. J. Serafin, 1980: Single- and multiple-Doppler radar observations of tornadic storms. *Mon. Wea. Rev.*, **108**, 1607–1625, doi:[10.1175/1520-0493\(1980\)108<1607:SAMDRO>2.0.CO;2](https://doi.org/10.1175/1520-0493(1980)108<1607:SAMDRO>2.0.CO;2).
- Rudlosky, S. D., and H. E. Fuelberg, 2013: Documenting storm severity in the mid-Atlantic region using lightning and radar information. *Mon. Wea. Rev.*, **141**, 3186–3202, doi:[10.1175/MWR-D-12-00287.1](https://doi.org/10.1175/MWR-D-12-00287.1).
- Rutledge, S. A., E. R. Williams, and T. D. Keenan, 1992: The Down Under Doppler and Electricity Experiment (DUNDEE): Overview and preliminary results. *Bull. Amer. Meteor. Soc.*, **73**, 3–16, doi:[10.1175/1520-0477\(1992\)073<0003:TDUDAE>2.0.CO;2](https://doi.org/10.1175/1520-0477(1992)073<0003:TDUDAE>2.0.CO;2).
- Saunders, C. P. R., H. Bax-Norman, C. Emersic, E. E. Avila, and N. E. Castellano, 2006: Laboratory studies of the effect of cloud conditions on graupel/crystal charge transfer in

- thunderstorm electrification. *Quart. J. Roy. Meteor. Soc.*, **132**, 2653–2673, doi:[10.1256/qj.05.218](https://doi.org/10.1256/qj.05.218).
- Schultz, C. J., 2015: Physical and dynamical control of lightning jumps and use for assessing severe thunderstorm potential. Ph.D. dissertation, University of Alabama in Huntsville, 208 pp.
- , W. A. Petersen, and L. D. Carey, 2009: Preliminary development and evaluation of lightning jump algorithms for the real-time detection of severe weather. *J. Appl. Meteor. Climatol.*, **48**, 2543–2563, doi:[10.1175/2009JAMC2237.1](https://doi.org/10.1175/2009JAMC2237.1).
- , —, and —, 2011: Lightning and severe weather: A comparison between total and cloud-to-ground lightning trends. *Wea. Forecasting*, **26**, 744–755, doi:[10.1175/WAF-D-10-05026.1](https://doi.org/10.1175/WAF-D-10-05026.1).
- , and Coauthors, 2012: Dual-polarization tornadic debris signatures Part I: Examples and utility in an operational setting. *Electron. J. Oper. Meteor.*, **13**, 120–137. [Available online at <http://www.nwas.org/ej/pdf/2012-EJ9.pdf>.]
- Scott, R. D., P. R. Krehbiel, and W. Rison, 2001: The use of simultaneous horizontal and vertical transmission for dual-polarization radar meteorological observations. *J. Atmos. Oceanic Technol.*, **18**, 629–648, doi:[10.1175/1520-0426\(2001\)018<0629:TUOSHA>2.0.CO;2](https://doi.org/10.1175/1520-0426(2001)018<0629:TUOSHA>2.0.CO;2).
- Stano, G. T., C. J. Schultz, L. D. Carey, D. R. MacGorman, and K. C. Calhoun, 2014: Total lightning observations and tools for the 20 May 2013 Moore, Oklahoma, tornadic supercell. *J. Oper. Meteor.*, **2**, 71–88, doi:[10.15191/nwajom.2014.0207](https://doi.org/10.15191/nwajom.2014.0207).
- Stough, S. M., L. D. Carey, and C. J. Schultz, 2015: Total lightning characteristics with respect to radar-derived mesocyclone strength. *Proc. Seventh Conf. on Meteorological Applications of Lightning Data*, Phoenix, AZ, Amer. Meteor. Soc., 11.2. [Available online at <https://ams.confex.com/ams/95Annual/webprogram/Paper258636.html>.]
- Stumpf, G. J., and Coauthors, 1998: The National Severe Storms Laboratory Mesocyclone Detection Algorithm for the WSR-88D. *Wea. Forecasting*, **13**, 304–326, doi:[10.1175/1520-0434\(1998\)013<0304:TNSSLM>2.0.CO;2](https://doi.org/10.1175/1520-0434(1998)013<0304:TNSSLM>2.0.CO;2).
- Tessendorf, S. A., L. J. Miller, K. C. Wiens, and S. A. Rutledge, 2005: The 29 June 2000 supercell observed during STEPS. Part I: Kinematics and microphysics. *J. Atmos. Sci.*, **62**, 4127–4150, doi:[10.1175/JAS3585.1](https://doi.org/10.1175/JAS3585.1).
- Tuttle, J. D., V. N. Bringi, H. D. Orville, and F. J. Kopp, 1989: Multiparameter radar study of a microburst: Comparison with model results. *J. Atmos. Sci.*, **46**, 601–620, doi:[10.1175/1520-0469\(1989\)046<0601:MRSOAM>2.0.CO;2](https://doi.org/10.1175/1520-0469(1989)046<0601:MRSOAM>2.0.CO;2).
- Vasiloff, S. V., E. A. Brandes, R. P. Davies-Jones, and P. S. Ray, 1986: An investigation of the transition from multicell to supercell storms. *J. Climate Appl. Meteor.*, **25**, 1022–1036, doi:[10.1175/1520-0450\(1986\)025<1022:AIOTTF>2.0.CO;2](https://doi.org/10.1175/1520-0450(1986)025<1022:AIOTTF>2.0.CO;2).
- Vivekanandan, J., D. S. Zrnic, S. M. Ellis, R. Oye, A. V. Rydzkow, and J. Straka, 1999: Cloud microphysics retrieval using S-band dual-polarization radar measurements. *Bull. Amer. Meteor. Soc.*, **80**, 381–388, doi:[10.1175/1520-0477\(1999\)080<0381:CMRUSB>2.0.CO;2](https://doi.org/10.1175/1520-0477(1999)080<0381:CMRUSB>2.0.CO;2).
- Wiens, K. C., S. A. Rutledge, and S. A. Tessendorf, 2005: The 29 June 2000 supercell observed during STEPS. Part II: Lightning and charge structure. *J. Atmos. Sci.*, **62**, 4151–4177, doi:[10.1175/JAS3615.1](https://doi.org/10.1175/JAS3615.1).
- Williams, E. R., M. E. Weber, and R. E. Orville, 1989: The relationship between lightning type and convective state of thunderclouds. *J. Geophys. Res.*, **94**, 13 213–13 220, doi:[10.1029/JD094iD11p13213](https://doi.org/10.1029/JD094iD11p13213).
- , and Coauthors, 1999: The behavior of total lightning activity in severe Florida thunderstorms. *Atmos. Res.*, **51**, 245–265, doi:[10.1016/S0169-8095\(99\)00011-3](https://doi.org/10.1016/S0169-8095(99)00011-3).
- Witt, A., M. D. Eilts, G. J. Stumpf, J. T. Johnson, E. D. Mitchell, and K. W. Thomas, 1998: An enhanced hail detection algorithm for the WSR-88D. *Wea. Forecasting*, **13**, 286–303, doi:[10.1175/1520-0434\(1998\)013<0286:AEHDAF>2.0.CO;2](https://doi.org/10.1175/1520-0434(1998)013<0286:AEHDAF>2.0.CO;2).
- Workman, E. J., and S. E. Reynolds, 1949: Electrical activity as related to thunderstorm cell growth. *Bull. Amer. Meteor. Soc.*, **30**, 142–144.
- Zipser, E. J., and K. R. Lutz, 1994: The vertical profile of radar reflectivity of convective cells: A strong indicator of storm intensity and lightning probability. *Mon. Wea. Rev.*, **122**, 1751–1759, doi:[10.1175/1520-0493\(1994\)122<1751:TVPORR>2.0.CO;2](https://doi.org/10.1175/1520-0493(1994)122<1751:TVPORR>2.0.CO;2).